

High-order two-fluid plasma solver for direct numerical simulations of plasma flows with full transport phenomena

Cite as: Phys. Plasmas **26**, 012109 (2019); <https://doi.org/10.1063/1.5082190>

Submitted: 19 November 2018 . Accepted: 28 December 2018 . Published Online: 22 January 2019

Z. Li , and D. Livescu 

COLLECTIONS

 This paper was selected as an Editor's Pick



View Online



Export Citation



CrossMark



High-order two-fluid plasma solver for direct numerical simulations of plasma flows with full transport phenomena

Cite as: Phys. Plasmas **26**, 012109 (2019); doi: [10.1063/1.5082190](https://doi.org/10.1063/1.5082190)

Submitted: 19 November 2018 · Accepted: 28 December 2018 · Published Online: 22 January 2019



View Online



Export Citation



CrossMark

Z. Li^{1,a)}  and D. Livescu^{2,b)} 

AFFILIATIONS

¹ Department of Engineering, Texas A&M University-Corpus Christi, Corpus Christi, Texas 78412, USA

² CCS-2, Los Alamos National Laboratory, Los Alamos, New Mexico 87545, USA

^{a)} Electronic mail: zhaorui.li@tamucc.edu

^{b)} Electronic mail: livescu@lanl.gov

ABSTRACT

The two-fluid plasma equations for a single ion species, with full transport terms, including temperature and magnetic field dependent ion and electron viscous stresses and heat fluxes, frictional drag force, and ohmic heating terms, have been implemented in the CFDNS code and solved by using sixth-order non-dissipative compact finite differences for plasma flows in several different regimes. In order to be able to fully resolve all the dynamically relevant time and length scales, while maintaining computational feasibility, the assumptions of infinite speed of light and negligible electron inertia have been made. Non-dimensional analysis of the two-fluid plasma equations shows that, by varying the characteristic/background number density, length scale, temperature, and magnetic strength, the corresponding Hall, resistive, and ideal magnetohydrodynamic equations can be recovered as limiting cases. The accuracy and robustness of this two-fluid plasma solver in handling plasma flows in different regimes have been validated against four canonical problems: Alfvén and whistler dispersion relations, electromagnetic plasma shock, and magnetic reconnection. For all test cases, by using physical dissipation and diffusion, with negligible numerical dissipation/diffusion, fully converged Direct Numerical Simulation (DNS)-like solutions are obtained when the ion Reynolds number based on the grid size is smaller than a threshold value which is about 2.3 in this study. For the magnetic reconnection problem, the results show that the magnetic flux saturation time and value converge when the ion and magnetic Reynolds numbers are large enough. Thus, the DNS-like results become relevant to practical problems with much larger Reynolds numbers.

Published under license by AIP Publishing. <https://doi.org/10.1063/1.5082190>

I. INTRODUCTION

Plasma, by far the most abundant form of ordinary matter in the universe, has been the subject of research in many disciplines, particularly in fusion,^{1–3} space physics,^{4–6} industrial applications,^{7–9} astrophysics,^{10–12} and so on. Aside from full *ab initio* descriptions,^{13–15} for many applications, a reasonable level of accuracy for plasma flow calculations can be achieved by using kinetic theory and the distribution functions that characterize each particle component.¹⁶ The evolution of the distribution functions is governed by the Boltzmann equation.¹⁷ However, for turbulent flows, solving the six-dimensional Boltzmann equation coupled with Maxwell's equations for the electromagnetic field is prohibitively expensive, due to the broad range of scales that need to be captured. Using the continuum approximation, when

possible, becomes computationally necessary for the description of turbulent plasma flows because the governing equations solved in the fluid model are three-dimensional. Assuming quasi-local thermal equilibrium (i.e., small departures from the Maxwellian distribution function) within each of the components, the fluid equations describing plasma dynamics can be obtained by taking appropriate moments of the Boltzmann equation and averaging over velocity space for each of the components.^{18,19}

For single component plasmas, i.e., consisting of electrons and a single ion component, starting from the equations for the ion and electron distribution functions, Braginskii¹⁷ derived a two-fluid hydrodynamic model for separate ion and electron fluids by using the Chapman-Enskog expansion with two-term

Sonine polynomial solutions. In the Braginskii two-fluid model, the transport terms include the magnetic field impact on the viscous stress tensor, heat flux, and frictional drag force, with different formulations along and perpendicular to the magnetic field. In contrast to the single ion component case, plasma equations containing multiple ion species involve additional transport phenomena such as baro- and electro-diffusion.^{20–22} Although this is a very active area of research,^{23–26} there are still many open questions, especially on how to treat mixtures with magnetic field dependent transport properties.

According to the H-theorem of Boltzmann,^{18,27} if the distribution function changes only by virtue of collisions, any arbitrary distribution will approach a Maxwellian. Therefore, the Braginskii two-fluid plasma model¹⁷ can describe well plasma flows in which the characteristic time scale is much larger than the collision time, i.e., $t_0 \gg \tau_s$, and the characteristic length scale is much larger than the distance traversed by particles between collisions (i.e., particle mean-free-path), i.e., $L_0 \gg \lambda_{\text{mfp}}$. One of such applications is the study of hydrodynamic instabilities between the hot spot and the colder surrounding plasma during the Inertial Confinement Fusion (ICF) coasting/deceleration stage. For the DT plasma in the early deceleration stage, the primary parameters of interest found in the literature,^{28,29} i.e., a reference number density of $n_0 \sim 10^{30} \text{m}^{-3}$, a temperature of $T_0 \sim 2.5 \text{keV}$, an acceleration of $g \sim 1.0 \times 10^{14} \text{m/s}^2$, and a hot-spot radius of $R_{\text{hs}} \approx 55 \mu\text{m}$, lead to $\tau_{\text{RT}}/\tau_i \approx 250 \gg 1$ and $R_{\text{hs}}/\lambda_{\text{mfp}} \approx 150 \gg 1$. Here, $\tau_{\text{RT}} = \sqrt{1/(Ak g)}$ is the classical single-mode Rayleigh-Taylor instability (RTI) growth time and τ_i is the ion collision time. The definitions of the Atwood number, A , and wavenumber, k , can be found in Ref. 30. Similarly, by using the typical plasma scales for the late deceleration stage,^{31,32} one obtains $\tau_{\text{RT}}/\tau_i \approx 500 \gg 1$ and $R_{\text{hs}}/\lambda_{\text{mfp}} \approx 320 \gg 1$.

Unfortunately, magnetized plasmas encountered in nature, including space and astrophysical plasmas, are mostly collisionless, and the typical collision time and mean-free-path in such flows can be comparable to or even larger than certain characteristic time and length scales of the flow. For example, according to the primary parameters given in Refs. 33 and 34, the particle mean-free-path in solar flare/corona is much larger than the length-scale of the reconnecting current sheet, i.e., $\lambda_{\text{mfp}} \approx 1.0 \times 10^5 \text{m} \gg \delta \sim 10 \text{m}$. Therefore, the quasi-Maxwellian distribution (or quasi-local thermal equilibrium) assumption does not seem to be guaranteed in such regimes. Theoretically, the highly collisionless magnetic reconnection can only be rigorously described by using collisionless kinetic models (e.g., Vlasov-Maxwell system of equations) in which both ion and electron kinetic-scale features are included.³⁵ However, in fact, the fluid model can still describe fairly well some strongly magnetized, collisionless plasma dynamics,^{1,36} which is largely due to the following two justifications. First, a strong magnetic field can play the role of collisions by forcing particles to gyrate in a Larmor orbit that is smaller than the mean free path by a factor of $\omega_{ce}\tau_e$,^{17,36} where ω_{ce} is the electron cyclotron frequency and τ_e is the electron collision time.¹ The other argument is that, even though the real distribution function in collisionless plasmas may significantly deviate from Maxwellian distribution, the fluid equations derived based on the quasi-Maxwellian assumption

may approach the physical solution when the range of fluid scales is very broad. This argument is similar to the mixing transition³⁷ often invoked in fluid turbulence to justify the relevance of finite Reynolds number simulations to practical problems with a much larger range of scales.³⁸ A more rigorous statement of the argument is that the flow develops an inertial range, where the energy cascade is local³⁹ and not influenced by the viscosity, except through the magnitude of the mean dissipation. From this point of view, it is tempting to assume that numerical dissipation in Euler equation simulations can act in a similar way and allow the development of an inertial range so that the numerical solution is close to the physical solution when the grid is fine enough. However, developing a power law range in the spectrum is not proof of the emergence of an inertial range⁴⁰ and proving cascade locality in the presence of numerical viscosity/diffusion may be impossible in general. In a broader sense, mixing transition may be extended to certain non-turbulent flows to mean convergence of the results with respect to the Reynolds number. In other instances, the concept of separation of scales can also be used to justify the relevance of fluid simulations to practical applications. For example, when the shock wave thickness is much smaller than the flow scales, the results become independent of the shock profile. In this case, even though the Navier-Stokes description breaks around strong shocks, it can still accurately predict the shock-turbulence interaction.⁴¹ While the mixing transition has not been explicitly explored for plasma flows, it has implicitly been assumed for example by showing that two-fluid plasma (including Hall-MHD) equations can successfully predict the fast reconnection rate in collisionless magnetic reconnection.^{6,42–45} Here, we further address this issue by considering the convergence of magnetic reconnection results as the ion and magnetic Reynolds numbers are increased.

Single-fluid magnetohydrodynamics (MHD) has been successfully used for studying large-scale plasma flows in a wide range of problems.^{46–51} However, single-fluid MHD fails to describe plasma phenomena that occur on a length scale comparable to or smaller than the ion skin depth, i.e., when $L_0 \leq \lambda_i = c/\omega_{pi}$, where c is the speed of light in vacuum and ω_{pi} is the ion plasma frequency. When applied to the magnetic reconnection problem, ideal MHD cannot predict the reconnection due to its flux-frozen-in limitation, while resistive MHD predicts a growth rate much lower than observations.⁶ This is because two-fluid effects become important at length scales below λ_i as the ion and electron motions start to decouple. By including the Hall current in the governing equations and electron pressure contribution to the total pressure, Hall-MHD equations⁵² account for some two-fluid effects and have been successful in capturing the rapid magnetic reconnection process.^{6,43,44,53} Nevertheless, Hall-MHD equations are not as general as the Braginskii two-fluid plasma model. For example, to close the Hall-MHD equations, some studies neglect the electron pressure altogether,^{54–56} while others assume identical ion and electron temperatures.^{34,57} In addition, when viscous effects were included in Hall-MHD equations,^{34,55} again these were less general than those in the Braginskii two-fluid plasma model.

In many practical problems, electron and ion temperatures are different. For example, the ion temperature in the Saturnian

magnetosphere near the Titan orbit is normally higher than the electron temperature, while in Titan's ionosphere, the electron temperature is dominant over the ion temperature.⁵⁸ The two-fluid plasma model^{17,46,59,60} can solve many of the problems encountered in single-fluid MHD and Hall-MHD formulations by considering separate ion and electron sets of equations. Nevertheless, previous applications of the two-fluid model^{59–61} did not include plasma transport terms and relied on the numerical dissipation/diffusion to obtain stable solutions; such solutions can obviously become corrupted by numerical artifacts and generally might misrepresent the physical transport.

Previous studies of plasma flows with physical transport phenomena such as thermal diffusion include simulations with Flash,^{62,63} Hydra,^{64,65} and Miranda^{29,66,67} codes. In these codes, the transport coefficients for thermal diffusion were calculated by using the Lee-More model.⁶⁸ However, Flash and Hydra codes solve the inviscid fluid equations and only Miranda explicitly considers viscous and diffusive effects.⁶⁹ In particular, the Miranda code uses a similar (even higher order) numerical scheme as the CFDNS code, with negligible numerical dissipation; however, this is accompanied by a high order filter to remove high frequency oscillations. No filtering is used with the CFDNS code. As far as we know, the magnetic field impact on the transport phenomena perpendicular to the magnetic field has not been considered in previous two-fluid plasma flow simulations. Nevertheless, the presence of a strong magnetic field reduces the distance traveled by particles between collisions. As a result, depending on the magnetic strength, plasma transport coefficients in the directions perpendicular to the magnetic field may become significantly small so that the associated fluxes are strongly anisotropic. As argued above, there are many situations, e.g., when a mixing transition exists, where the exact form of the physical transport is not important, provided that the energy transfer among scales of motion remains local. Nevertheless, such transition and the role of anisotropic transport have not been explored for many of the practical situations of interest.

The objective of this study is to present an accurate two-fluid plasma solver with a single ion component that can simulate magnetized plasma flows in a range of applications, with a special focus on collisional dominated transport for low-Z fully ionized nondegenerate plasmas, in regimes where the results might be sensitive to the exact formulation of the transport terms. All plasma transport terms such as the temperature and magnetic field dependent ion and electron viscous stresses and heat fluxes, frictional drag force, and ohmic heating are included in the two-fluid plasma solver. To obtain fully resolved Direct Numerical Simulation (DNS)-like solutions, the two-fluid plasma equations are solved by using sixth-order non-dissipative compact finite differences⁷⁰ at sufficiently fine grid resolutions. In this study, to maintain computational feasibility, the infinite speed of light and negligible electron inertia assumptions are made to eliminate severe time-step limitations. These two assumptions can be well justified for problems such as the ICF coasting stage, where ion thermal velocity is non-relativistic, $V_{Ti}/c \sim O(10^{-3})$, and $m_i/m_e \sim 5 \times 10^3$. The length scale limitation imposed by using these two assumptions, $L_0 \gg (r_{Le}, \lambda_e)$,

where r_{Le} is the electron Larmor radius and λ_e is the electron skin depth, is also satisfied in many other practical problems. While the primary target applications for the new solver are plasma flows which can be described with collisional transport terms, the test problems considered are widely used in the literature and have been addressed primarily using ideal equations solvers; the numerical treatment of such equations requires numerical dissipation/diffusion for regularization. Our new solver yields smooth solutions without any numerical dissipation/diffusion and can recover inviscid analytical solutions for sufficiently high Reynolds numbers.

In general, the Braginskii transport coefficients become inaccurate for degenerate partially ionized plasmas or high-Z materials.⁶⁸ However, more general formulations do not include the full directional dependence of the physical transport with respect to the magnetic field. A separate objective of this study is to form the basis of future estimations of anisotropic transport importance and explore the existence of a mixing transition in various applications.

This paper is organized as follows: in Sec. II, the derivations of reduced two-fluid plasma equations from the Braginskii full two-fluid plasma model, together with an analysis of their ranges of applicability, are discussed in detail. A non-dimensional analysis of the reduced two-fluid plasma equations is conducted in Sec. III. The accuracy and robustness of the two-fluid plasma solver are highlighted, in Sec. IV, against a series of canonical problems. Finally, the main conclusions are provided in Sec. V.

II. MATHEMATICAL FORMULATION

The macroscopic description of plasma in fluid theory can be obtained by taking appropriate moments of the Boltzmann equation and averaging over velocity space for each of the components in plasma. When using the Chapman-Enskog expansion,^{18,19} the zeroth-order distribution function for each species, f_s^0 , is chosen to be a Maxwellian, which assumes a local thermal equilibrium within each of the components. By considering the effects that produce small deviations from equilibrium, Braginskii¹⁷ derived a set of two-fluid plasma transport equations and constitutive relations for all transport terms. On the other hand, ignoring those effects leads to a set of Euler-type two-fluid plasma equations in which all transport phenomena are absent.^{59,60} Such equations develop singularities in finite time and need to be regularized by the numerical algorithm.

A. Braginskii's two-fluid plasma model

For a simple fully ionized plasma, the continuity, momentum, and internal energy transport equations for species s ($s = i$ for ions and $s = e$ for electrons) are given as follows:¹⁷

$$\frac{\partial \rho_s}{\partial t} + \nabla \cdot (\rho_s \mathbf{u}_s) = 0, \quad (1)$$

$$\begin{aligned} \frac{\partial (\rho_s \mathbf{u}_s)}{\partial t} + \nabla \cdot (\rho_s \mathbf{u}_s \mathbf{u}_s) \\ = -\nabla p_s - \nabla \cdot \boldsymbol{\pi}_s + \frac{q_s \rho_s}{m_s} (\mathbf{E} + \mathbf{u}_s \times \mathbf{B}) + \mathbf{R}_s + \rho_s \mathbf{g}, \end{aligned} \quad (2)$$

$$\frac{\partial (\rho_s e_s)}{\partial t} + \nabla \cdot (\rho_s e_s \mathbf{u}_s) = -p_s \nabla \cdot \mathbf{u}_s - \nabla \cdot \mathbf{q}_s + \boldsymbol{\pi}_s : \nabla \mathbf{u}_s + Q_s, \quad (3)$$

where the primary variables are species density, ρ_s , velocity, \mathbf{u}_s , and specific internal energy, e_s . In this study, the ideal gas equation of state (EOS) is assumed for simplicity. Therefore, the species pressure can be expressed as $p_s = (\gamma - 1)\rho_s e_s = n_s k_B T_s$, in which γ and k_B are the specific heat ratio and Boltzmann constant, while $n_s = \rho_s/m_s$ and T_s are the species number density and temperature, respectively. m_s and q_s are the mass and charge of particle s . The ion and electron charges are $q_i = Ze$ and $q_e = -e$, in which e is the constant elementary charge. The formulations for plasma transport terms in the above equations, including species viscous stress, $\boldsymbol{\pi}_s$, heat flux, \mathbf{q}_s , frictional drag force, \mathbf{R}_s , and collision generated heat, Q_s , can be found in [Appendix A](#) and [Ref. 17](#). The accuracy of Braginskii transport coefficients for the domain of applicability has been confirmed by comparing with the transport coefficients predicted by using *Ab Initio* Molecular Dynamics (AIMD).^{71,72} For example, for the DT hot-spot in ICF with a number density of $n_e \sim 10^{31} \text{m}^{-3}$ and a temperature of $T_e \sim 10.0 \text{keV}$, the electron thermal conductivity calculated by using the Braginskii model (see [Appendix A](#) for full definitions) is $\kappa_{Te} = n_e k_B^2 T_e \tau_e / m_e = (n_e k_B^2 T_e / m_e) \times [6\sqrt{2}\pi^{3/2} \epsilon_0^2 \sqrt{m_e} (k_B T_e)^{3/2} / (\ln \Lambda e^4 Z n_e)] \approx 5.15 \times 10^9 (\text{Wm}^{-1} \text{K}^{-1})$ which is very close to the AIMD prediction,⁷² i.e., $\kappa_e = 5.05 \times 10^9 (\text{Wm}^{-1} \text{K}^{-1})$.

As discussed before, the Braginskii two-fluid plasma model is derived for the collision-dominated plasma flows in which the characteristic time and length scales are much larger than the collision time and the particle mean-free-path, i.e., $t_0 \gg \tau_s$ and $L_0 \gg \lambda_{\text{mfp}}$. In addition, the Braginskii transport coefficients become inaccurate for degenerate partially ionized or high-Z plasmas.⁶⁸ Thus, the results presented here apply to fully ionized nondegenerate single low-Z ion component collisional plasmas or plasma flows where a mixing transition has occurred.

The evolutions of electric field, \mathbf{E} , and magnetic field, \mathbf{B} , are governed by the Maxwell equations given as follows:

$$\frac{1}{c^2} \frac{\partial \mathbf{E}}{\partial t} = \nabla \times \mathbf{B} - \mu_0 \mathbf{J}, \quad (4)$$

$$\frac{\partial \mathbf{B}}{\partial t} = -\nabla \times \mathbf{E}, \quad (5)$$

$$\nabla \cdot \mathbf{E} = \frac{\rho_c}{\epsilon_0}, \quad (6)$$

$$\nabla \cdot \mathbf{B} = 0, \quad (7)$$

where μ_0 and ϵ_0 are the permeability and permittivity of free space, respectively, and are related to the speed of light in vacuum, c , as $c = (\mu_0 \epsilon_0)^{-1/2}$. In the above equations, the formulations for current density, \mathbf{J} , and local charge density, ρ_c , are $\mathbf{J} = \sum q_s n_s \mathbf{u}_s = e(Zn_i \mathbf{u}_i - n_e \mathbf{u}_e)$ and $\rho_c = \sum q_s n_s = e(Zn_i - n_e)$, respectively. It is worth pointing out that, for closing the governing equations, one only needs to solve two of the Maxwell equations and the other two equations [e.g., Eqs. (6) and (7)] are just restatements of the closed set of governing equations. For example, by multiplying continuity Eq. (1) by q_s/m_s and then taking summation over ion ($s = i$) and electron ($s = e$) species, one obtains

$$\frac{\partial \rho_c}{\partial t} + \nabla \cdot \mathbf{J} = 0. \quad (8)$$

Furthermore, by taking the divergence of Ampere Eq. (4) and then subtracting it from Eq. (8), it yields

$$\frac{\partial}{\partial t} (\nabla \cdot \mathbf{E} - \rho_c / \epsilon_0) = 0. \quad (9)$$

Obviously, the Gauss equation (6) is just a restatement of the consequence [i.e., Eq. (9)] of solving continuity Eq. (1) and Ampere Eq. (4). In this study, we would like to call Eq. (6) a diagnostic equation instead of a redundant equation. This is because that, after applying the two assumptions discussed in [Secs. II B](#) and [II C](#), the electric field is calculated from generalized Ohm's law (13) instead of the Ampere equation (4), and Eq. (8) is reduced to a quasi-neutrality condition. As a result, Eq. (9) is no longer rigorously guaranteed to be satisfied when solving the final governing equations given in [Sec. II D](#). Therefore, in this study, we solve Eq. (6) as a diagnostic tool to monitor the importance of the numerical integration errors. By following the same procedure, one can also conclude that, mathematically, the magnetic field remains divergence free if it is initially divergence free.

B. Infinite speed of light assumption

In this study, the severe time-step restrictions⁵⁷ (e.g., $\Delta t \leq \text{CFL} \Delta x / c$ and $\Delta t \leq 0.1 / \omega_{pe}$, where CFL is the Courant-Frederich-Levy constant, Δx is the mesh size, and ω_{pe} is the electron plasma frequency) caused by high frequency electromagnetic waves are eliminated by using the infinite speed of light assumption, i.e., $(\partial \mathbf{E} / \partial t) / c^2 \approx 0$, which reduces the Amperes equation (4) to

$$\mathbf{J} = \frac{1}{\mu_0} \nabla \times \mathbf{B}. \quad (10)$$

Consequently, this assumption restricts the calculations to plasma flows with nonrelativistic thermal velocity, $V_{Ts} = \sqrt{k_B T_s / m_s} \ll c$, and to electromagnetic waves with phase speed, $V_p = \omega / k \ll c$ (also see [Ref. 46](#)). Furthermore, by substituting Eq. (10) into Eq. (8), one obtains

$$\frac{\partial \rho_c}{\partial t} = 0, \quad (11)$$

which indicates that the quasi-neutrality condition ($\rho_c = 0$) is maintained at all times if the initial plasma flow is charge free. Consistently, the number densities and mass densities of ions and electrons become dependent, i.e., $n_e = Zn_i$ and $\rho_e = Z(m_e / m_i) \rho_i$, which eliminates the need to solve the continuity equation (1) for electrons and relates the ion and electron velocities via the current density as

$$\mathbf{u}_e = \mathbf{u}_i - \left(\frac{1}{eZn_i} \right) \mathbf{J}. \quad (12)$$

The quasi-neutrality condition limits our interest to plasma phenomena whose characteristic frequency is much smaller than the electron plasma frequency, $\omega \ll \omega_{pe} = \sqrt{n_e e^2 / \epsilon_0 m_e}$, and characteristic length is much larger than the Debye length, $L_0 \gg \lambda_{De} = V_{Te} / \omega_{pe}$ (also see [Ref. 46](#)).

C. Negligible electron inertia assumption

The second assumption made in this study is negligible electron inertia in the electron momentum equation (2). This

assumption is justified as the right-hand side of the electron momentum equation is of the same order as that of the ion momentum equation, but the advection part is of the order m_e/m_i compared to the corresponding part of the ion momentum equation. Then, after applying the relation between ion and electron velocities [Eq. (12)], one can obtain generalized Ohm's law as

$$\mathbf{E} = \left(\frac{m_i}{eZ\rho_i} \right) \left[-\nabla p_e - \nabla \cdot \boldsymbol{\pi}_e + \mathbf{R}_e + Z \left(\frac{m_e}{m_i} \right) \rho_i \mathbf{g} + \mathbf{J} \times \mathbf{B} \right] - \mathbf{u}_i \times \mathbf{B}, \quad (13)$$

where the Biermann battery, viscous, resistive, acceleration, and Hall effects are all included. Recent kinetic simulations²⁰ show that the Biermann battery term appearing in Eq. (13) is the physical source of strong, self-generated electric fields observed in ICF plasma.⁷³ The rest of the terms, in particular, the Hall term and the last term in Eq. (13), are also indispensable in maintaining the constant charge condition [i.e., Eq. (11)].

Negligible electron inertia implies that the electron flow has an infinite fast response time on the time scales of interest. Therefore, the characteristic time scale of interest must be larger than electron plasma frequency and electron cyclotron frequency, i.e., $1/\omega \gg (1/\omega_{pe}, 1/\omega_{ce})$, which further relaxes the time-step restriction on $0.1/\omega_{ce}$.⁵⁷ Consistently, the characteristic length scale of interest must be longer than the Debye length, the electron Larmor radius, and/or the electron skin depth, i.e., $L_0 \gg (\lambda_{De}, r_{Le}, \text{ and/or } \lambda_e)$, where $r_{Le} = V_{Te}/\omega_{ce}$, $\lambda_e = V_A/\omega_{ce} = c/\omega_{pe}$, and $V_A = B/\sqrt{\mu_0 n_i m_i}$ is the ion Alfvén velocity. The infinite speed of light assumption further reduces the above condition to $L_0 \gg (r_{Le} \text{ and/or } \lambda_e)$ since $\lambda_e/\lambda_{De} = c/V_{Te} \gg 1$.

After replacing the electric field, \mathbf{E} , in the momentum equation (2) for ions using Eq. (13) and then applying the quasi-neutrality condition, a modified expression for the ion momentum equation can be written as

$$\frac{\partial(\rho_i \mathbf{u}_i)}{\partial t} + \nabla \cdot (\rho_i \mathbf{u}_i \mathbf{u}_i) = -\nabla(p_i + p_e) - \nabla \cdot (\boldsymbol{\pi}_i + \boldsymbol{\pi}_e) + (\mathbf{R}_e + \mathbf{R}_i) + \mathbf{J} \times \mathbf{B} + \rho_i \mathbf{g}. \quad (14)$$

D. Final two-fluid plasma equations

Finally, the two-fluid plasma transport equations considered in this study are the dimensional ion continuity equation, ion momentum equation, ion and electron internal energy equations, and Faraday's law, and are summarized as follows:

$$\frac{\partial \rho_i}{\partial t} + \nabla \cdot (\rho_i \mathbf{u}_i) = 0, \quad (15)$$

$$\frac{\partial(\rho_i \mathbf{u}_i)}{\partial t} + \nabla \cdot (\rho_i \mathbf{u}_i \mathbf{u}_i) = -\nabla(p_i + p_e) - \nabla \cdot (\boldsymbol{\pi}_i + \boldsymbol{\pi}_e) + \mathbf{J} \times \mathbf{B} + \rho_i \mathbf{g}, \quad (16)$$

$$\frac{\partial(\rho_i e_i)}{\partial t} + \nabla \cdot (\rho_i e_i \mathbf{u}_i) = -p_i \nabla \cdot \mathbf{u}_i - \nabla \cdot \mathbf{q}_i + \boldsymbol{\pi}_i : \nabla \mathbf{u}_i + Q_\Delta, \quad (17)$$

$$\frac{\partial(\rho_i e_e)}{\partial t} + \nabla \cdot (\rho_i e_e \mathbf{u}_e) = \left(\frac{m_i}{Z m_e} \right) \left[-p_e \nabla \cdot \mathbf{u}_e - \nabla \cdot \mathbf{q}_e + \boldsymbol{\pi}_e : \nabla \mathbf{u}_e + \left(\frac{m_i}{eZ\rho_i} \right) \mathbf{R}_e \cdot \mathbf{J} - Q_\Delta \right], \quad (18)$$

$$\frac{\partial \mathbf{B}}{\partial t} = -\nabla \times \mathbf{E}, \quad (19)$$

where the current density, \mathbf{J} , electron velocity, \mathbf{u}_e , and electric field, \mathbf{E} , are calculated from formulations (10), (12), and (13), respectively. The ion/electron pressures, p_s , and temperatures, T_s , are related through the ideal gas EOS as described in Sec. II A.

As a result of infinite speed of light and negligible electron inertia assumptions, the consistency of the quasi-neutrality condition ($\rho_c \approx 0$) in the final two-fluid plasma equations must be checked numerically by examining the value of charge density, ρ_c , calculated from Eq. (6). In other words, the divergence of the electric field, \mathbf{E} , calculated from generalized Ohm's law Eq. (13) must be sufficiently small to maintain the quasi-neutrality condition. The numerical results obtained for all test cases confirm the quasi-neutrality condition, and two sample results are presented in Appendix B.

III. NON-DIMENSIONAL ANALYSIS

In order to assess the importance of Hall and Biermann battery effects, resistivity, viscous stress, and heat flux in plasma flows in different regimes, as well as characterize special limiting cases, in this section, a non-dimensional analysis of the two-fluid plasma equations is provided. In order to compare different applications, the characteristic parameters that can be varied in practical problems of interest including temperature, number density, characteristic length scale, and magnetic field strength are chosen as the primary reference quantities.

A. Non-dimensional two-fluid plasma equations

We choose the characteristic number density, n_0 , length scale, L_0 , temperature, T_0 , magnetic field strength, B_0 , and external acceleration, g_0 , as the primary reference quantities and use them to construct scales for other variables like ion mass density, $\rho_0 = n_0 m_i$, ion Alfvén velocity, $V_A^0 = B_0/\sqrt{\mu_0 n_0 m_i}$, plasma pressure, $p^0 = n_0 k_B T_0$, a time scale, L_0/V_A^0 , and so on. With these choices, the non-dimensional two-fluid plasma equations become

$$\frac{\partial \rho_i^*}{\partial t^*} + \nabla^* \cdot (\rho_i^* \mathbf{u}_i^*) = 0, \quad (20)$$

$$\begin{aligned} \frac{\partial(\rho_i^* \mathbf{u}_i^*)}{\partial t^*} + \nabla^* \cdot (\rho_i^* \mathbf{u}_i^* \mathbf{u}_i^*) &= -\beta \nabla^* (p_i^* + p_e^*) + \mathbf{J}^* \times \mathbf{B}^* \\ &\quad - \frac{1}{\text{Re}^i} \nabla^* \cdot \boldsymbol{\pi}_i^* - \frac{1}{\text{Re}^e} \nabla^* \cdot \boldsymbol{\pi}_e^* + \frac{1}{\text{Fr}^2} \rho_i^* \mathbf{g}^*, \end{aligned} \quad (21)$$

$$\begin{aligned} \frac{\partial(\rho_i^* e_i^*)}{\partial t^*} + \nabla^* \cdot (\rho_i^* e_i^* \mathbf{u}_i^*) &= -\beta p_i^* \nabla^* \cdot \mathbf{u}_i^* - \frac{\beta}{\text{Re}^i} \nabla^* \cdot \mathbf{q}_i^* \\ &\quad + \frac{1}{\text{Re}^i} \boldsymbol{\pi}_i^* : \nabla^* \mathbf{u}_i^* + 3Z \left(\frac{m_i}{m_e} \right) \beta \omega_{ei}^0 Q_\Delta^*, \end{aligned} \quad (22)$$

$$\frac{\partial(\rho_i^* e_e^*)}{\partial t^*} + \nabla^* \cdot (\rho_i^* e_e^* \mathbf{u}_e^*) = \left(\frac{m_i}{Z m_e} \right) \left[-\beta p_e^* \nabla^* \cdot \mathbf{u}_e^* - \left(\frac{m_i}{m_e} \right) \frac{\beta}{\text{Re}^e} \nabla^* \cdot \mathbf{q}_{Te}^* - \frac{1}{\text{Re}^e} \pi_e^* : \nabla^* \mathbf{u}_e^* + \frac{1}{\text{Re}_m} \mathbf{R}_u^* \cdot \mathbf{J}^* \right] - 3\omega_{ei}^0 \beta Q_\Delta^* + \left(\frac{m_i}{m_e} \right) \hat{\lambda}_i \beta (-\nabla^* \cdot \mathbf{q}_{ue}^* + \mathbf{R}_T^* \cdot \mathbf{J}^*), \quad (23)$$

$$\frac{\partial \mathbf{B}^*}{\partial t^*} = -\nabla^* \times \mathbf{E}^*, \quad (24)$$

$$\mathbf{E}^* = \hat{\lambda}_i \frac{1}{\rho_i^*} \left[\mathbf{J}^* \times \mathbf{B}^* - \beta \nabla^* p_e^* - \frac{1}{\text{Re}^e} \nabla^* \cdot \pi_e^* + Z \beta \rho_i^* \mathbf{R}_T^* + \left(\frac{Z m_e}{m_i} \right) \frac{1}{\text{Fr}^2} \rho_i^* \mathbf{g}^* \right] + \frac{1}{\text{Re}_m} \mathbf{R}_u^* - \mathbf{u}_i^* \times \mathbf{B}^*, \quad (25)$$

$$\mathbf{u}_e^* = \mathbf{u}_i^* - \hat{\lambda}_i \frac{1}{\rho_i^*} \mathbf{J}^*, \quad (26)$$

$$\mathbf{J}^* = \nabla^* \times \mathbf{B}^*. \quad (27)$$

where the superposed asterisk refers to the dimensionless variable and the non-dimensional parameters are the ion inertial scale or skin depth

$$\hat{\lambda}_i = c / (\omega_{pi}^0 L_0) = m_i / (Z e L_0 \sqrt{\mu_0 \rho_0}), \quad (28)$$

ion and electron reference Reynolds (or viscous Lundquist) numbers

$$\text{Re}^i = \rho_0 V_A^0 L_0 / \mu_i^0, \quad (29)$$

$$\text{Re}^e = (\mu_i^0 / \mu_e^0) \text{Re}^i, \quad (30)$$

plasma beta

$$\beta = n_0 k_B T_0 / (B_0^2 / \mu_0), \quad (31)$$

magnetic Reynolds (or resistive Lundquist) number

$$\text{Re}_m = \mu_0 V_A^0 L_0 / \eta^0. \quad (32)$$

Froude number, and

$$\text{Fr} = V_A^0 / \sqrt{g_0 L_0}, \quad (33)$$

the collision frequency

$$\omega_{ei}^0 = L_0 / (V_A^0 \tau_e^0). \quad (34)$$

In the above non-dimensional parameters, $\eta^0 = \left(\frac{m_i}{e Z \rho_0} \right) \times \left(\frac{m_e}{e \tau_e^0} \right)$ is the background resistivity, and the formulations for other reference variables are ion plasma frequency, $\omega_{pi}^0 = Z e \sqrt{n_0 / (\epsilon_0 m_i)}$, ion viscosity, $\mu_i^0 = n_0 k_B T_0 \tau_i^0$, electron viscosity, $\mu_e^0 = Z n_0 k_B T_0 \tau_e^0$, ion collision time, $\tau_i^0 = [12 \pi^{3/2} \epsilon_0^2 \sqrt{m_i} (k_B T_0)^{3/2} / (\ln \Lambda e^4 Z^4 n_0)]$, and electron collision time, $\tau_e^0 = [6 \sqrt{2} \pi^{3/2} \epsilon_0^2 \sqrt{m_e} (k_B T_0)^{3/2} / (\ln \Lambda e^4 Z^2 n_0)]$. The Coulomb logarithm ($\ln \Lambda$) variation is described in [Appendix A](#).

In addition, by using the relations, $r_{Le} / r_{Li} = \lambda_e / \lambda_i = \sqrt{m_e / m_i}$, we can summarize the range of applicability for the two assumptions made in this study in terms of the non-dimensional ion length scales as: $\hat{\lambda}_i \ll \sqrt{m_i / m_e}$ and/or

$\hat{r}_{Li} \ll \sqrt{m_i / m_e}$ depending on the local magnetic field strength. Thus, in the magnetic dominant regime (e.g., low plasma β), the fact that $\hat{r}_{Li} / \hat{\lambda}_i = \sqrt{\beta} < 1$ yields $\hat{\lambda}_i \ll \sqrt{m_i / m_e}$. On the other hand, in the plasma dominant regime (e.g., large plasma β), the applicability condition becomes $\hat{r}_{Li} \ll \sqrt{m_i / m_e}$.

B. Single-fluid limiting equations

In order to demonstrate the limiting cases of the two-fluid plasma equations solved in this study, the non-dimensional single-fluid plasma equations for ion-electron mixture density $\rho^* = \rho_i^* + \rho_e^*$, velocity, $\mathbf{u}^* = (\rho_i^* \mathbf{u}_i^* + \rho_e^* \mathbf{u}_e^*) / \rho^*$, and pressure, $p^* = p_i^* + p_e^*$, are derived from the two-fluid plasma equations and given as follows:

$$\frac{\partial \rho^*}{\partial t^*} + \nabla^* \cdot (\rho^* \mathbf{u}^*) = 0, \quad (35)$$

$$\frac{\partial(\rho^* \mathbf{u}^*)}{\partial t^*} + \nabla^* \cdot (\rho^* \mathbf{u}^* \mathbf{u}^*) = -\beta \nabla^* p^* + \mathbf{J}^* \times \mathbf{B}^* - \frac{1}{\text{Re}^i} \nabla^* \cdot \pi_i^* - \frac{1}{\text{Re}^e} \nabla^* \cdot \pi_e^* + \frac{1}{\text{Fr}^2} \rho^* \mathbf{g}^*, \quad (36)$$

$$\begin{aligned} \frac{1}{\gamma - 1} \left[\frac{\partial p^*}{\partial t^*} + \nabla^* \cdot (p^* \mathbf{u}^*) \right] &= -p^* \nabla^* \cdot \mathbf{u}^* + \frac{\hat{\lambda}_i}{\gamma - 1} \nabla^* \cdot \left(\frac{p_e^*}{\rho_i^*} \mathbf{J}^* \right) \\ &+ \hat{\lambda}_i p_e^* \nabla^* \cdot \left(\frac{\mathbf{J}^*}{\rho_i^*} \right) + \frac{1}{\beta \text{Re}_m} \mathbf{R}_u^* \cdot \mathbf{J}^* \\ &- \left(\frac{1}{\text{Re}^i} \nabla^* \cdot \mathbf{q}_i^* + \frac{m_i}{m_e} \frac{1}{\text{Re}^e} \nabla^* \cdot \mathbf{q}_{Te}^* \right) \\ &- \frac{1}{\beta} \left(\frac{1}{\text{Re}^i} \pi_i^* : \nabla^* \mathbf{u}_i^* + \frac{1}{\text{Re}^e} \pi_e^* : \nabla^* \mathbf{u}_e^* \right) \\ &+ Z \hat{\lambda}_i (-\nabla^* \cdot \mathbf{q}_{ue}^* + \mathbf{R}_T^* \cdot \mathbf{J}^*). \end{aligned} \quad (37)$$

Equation (35) is obtained by applying the relations $\rho_e^* / \rho_i^* = Z m_e / m_i$, $\rho^* = \rho_i^* + \rho_e^*$, $\mathbf{u}^* = (\rho_i^* \mathbf{u}_i^* + \rho_e^* \mathbf{u}_e^*) / \rho^*$, and Eqs. (26) and (27) into Eq. (20). Similarly, by using the above ion-electron mixture variable definitions (including $p^* = p_i^* + p_e^*$) and Eq. (26), one can obtain Eq. (36) from the ion momentum equation (21) under the negligible electron inertia assumption. Finally, using the non-dimensional EOS, $\rho_s^* e_s^* = \beta / (\gamma - 1) p_s^*$, the ion-electron mixture variable definitions, negligible electron inertia assumption, and Eq. (26), Eq. (37) is obtained by taking summation of ion and electron energy Eqs. (22) and (23).

In addition, generalized Ohm's law is rewritten as

$$\mathbf{E}^* + \mathbf{u}^* \times \mathbf{B}^* = \hat{\lambda}_i \frac{1}{\rho_i^*} \mathbf{J}^* \times \mathbf{B}^* - \hat{\lambda}_i \frac{\beta}{\rho_i^*} \nabla^* p_e^* + \frac{1}{\text{Re}_m} \mathbf{R}_u^* - \hat{\lambda}_i \frac{1}{\rho_i^* \text{Re}^e} \nabla^* \cdot \pi_e^* + Z \hat{\lambda}_i \beta \mathbf{R}_T^* + \hat{\lambda}_i \frac{Z}{\text{Fr}^2} \frac{m_e}{m_i} \mathbf{g}^*. \quad (38)$$

Equation (38) is obtained by substituting the ion-electron mixture variables and Eq. (26) into Eq. (25). Faraday's law for the non-dimensional magnetic field, \mathbf{B}^* , and reduced Ampere's law for current density, \mathbf{J}^* , remain unchanged as Eqs. (24) and (27), respectively.

The ion velocity \mathbf{u}_i^* and electron velocity \mathbf{u}_e^* can be obtained by using the relations $\rho_e^* / \rho_i^* = Z m_e / m_i$, $\rho^* = \rho_i^* + \rho_e^*$, $\mathbf{u}^* = (\rho_i^* \mathbf{u}_i^* + \rho_e^* \mathbf{u}_e^*) / \rho^*$, and the definition of current density under quasi-neutrality condition (26) and then are used to calculate the

viscous stresses, π_e^* and π_i^* , appearing in the single-fluid equations (36)–(38).

Written as above, the equations are unclosed, as the ion and electron temperatures and densities cannot be independently determined. For plasma flows with identical ion and electron temperatures (i.e., $T_i^* = T_e^*$), the ion and electron temperatures become the same as the mixture temperature, T^* , which can be obtained from the total pressure, p^* , by using the EOS. In addition, the electron pressure can be obtained via the relation $p_e^* = Zp_i^* = p^*/(1 + 1/Z)$. In this case, the single-fluid plasma equations, including all transport terms, are closed.

As demonstrated in Appendix C, the conventional Hall, resistive, and ideal MHD equations can be recovered from the above single-fluid plasma equations, as limiting cases, in regimes where the non-dimensional parameters satisfy the corresponding conditions described below:

- The conventional Hall-MHD equations can be recovered in regimes where $Re^i, Re^e \rightarrow \infty, Fr \rightarrow \infty, \mathbf{q}_{\text{he}}^* \rightarrow 0$, and $\mathbf{R}_T^* \rightarrow 0$ (\mathbf{q}_{he}^* and \mathbf{R}_T^* are always ignored in the Hall-MHD equations and are only considered in the Braginskii two-fluid model¹⁷)
- Resistive MHD equations can be recovered in regimes where $\hat{\lambda}_i \rightarrow 0$ (and/or $\hat{r}_{Li} \rightarrow 0$), $Re^i, Re^e \rightarrow \infty$, and $Fr \rightarrow \infty$.
- Ideal MHD equations can be recovered in regimes where $\hat{\lambda}_i \rightarrow 0$ (and/or $\hat{r}_{Li} \rightarrow 0$), $Re^i, Re^e \rightarrow \infty, Fr \rightarrow \infty$, and $Re_m \rightarrow \infty$.

The Hall-MHD equations can sometimes be classified as a two-fluid model because of the inclusion of the Hall term and the electron pressure gradient. However, similar to the discussion made above, due to the presence of the electron pressure, the Hall-MHD equations are not closed. In practice, to close the Hall-MHD equations, some studies^{54–56} simply neglect the electron pressure, while others^{34,57} assume identical ion and electron temperatures ($T_i^* = T_e^*$) and obtain the electron pressure as $p_e^* = Zp_i^* = p^*/(1 + 1/Z)$.

The viscous terms vanish from the single-fluid equations in the limit of infinite Reynolds numbers only for non-turbulent flows. This restricts the domain of applicability of the limiting cases above, unless models for subgrid or turbulence transport are added to the equations. In some recent studies,^{34,55} viscous effects are included in the Hall-MHD equations for regimes where Re^i is not sufficiently large. However, the formulations for the viscous terms are more or less ad-hoc. Some studies⁵⁵ model the viscous stress term by using ion–electron mixture velocity, \mathbf{u}^* , with the standard formulation for compressible ideal gas, i.e., $\nabla^* \cdot \boldsymbol{\pi}^* = \nabla^{*2} \mathbf{u}^* + (1/3) \nabla^* \nabla^* \cdot \mathbf{u}^*$ instead of the detailed plasma formulations for π_i^* and π_e^* given in Appendix A. In addition, the viscous contribution was only added to the momentum equations.

In Sec. IV, numerical simulations will be conducted for a series of canonical problems to highlight the accuracy and robustness of the two-fluid plasma solver in handling plasma flows in different regimes.

IV. TEST CASES

The dimensional two-fluid plasma equation with full transport terms described in Sec. IID have been implemented in the

CFDNS code^{41,74,75} and solved by using sixth-order non-dissipative compact finite differences^{70,75} for four canonical problems: Alfvén and whistler dispersion relations, electromagnetic plasma shock, and magnetic reconnection. For these cases, ion and electron temperatures are the same, i.e., $T_i = T_e$. Therefore, the collision generated heat for the ion energy equation, $Q_i(Q_\Delta)$, vanishes, while the collision generated heat for the electron energy equation, Q_e , reduces to the ohmic heating term shown as the fourth term in the RHS of Eq. (18). Therefore, the two-fluid plasma equations solved in these test cases are mathematically equivalent to the single-fluid plasma equations described in Sec. III B which can be viewed as the general or full Hall-MHD equations (therefore more general than the conventional Hall-MHD equations used in previous studies and explained in Appendix C 1), including all plasma transport terms. The identical temperature simplification further eliminates the need to solve the ion energy equation (17).

For the test cases considered in this study, the initial conditions for all primary variables (non-dimensional) are identical to those given in the references mentioned below. The values of the non-dimensional parameters, i.e., $\hat{\lambda}_i$, Re^i , and Re_m , are calculated based on the characteristic number density, n_0 , length scale, L_0 , temperature, T_0 , and magnetic strength, B_0 , and chosen to match previous studies and/or certain practical applications, with the requirement that the simulations remain well-resolved.

A. Alfvén and whistler dispersion relations

The first two test cases used to test the accuracy of the newly developed two-fluid plasma solver are the dispersion relations for Alfvén and whistler waves. These are the two plasma phenomena often observed in different space flow regimes.^{4,76–78} The frequency and length scales for Alfvén waves satisfy the relations $\omega \ll \omega_{ci}$ and $L_0 \gg c/\omega_{pi} = \lambda_i$.⁷⁹ Therefore, Alfvén waves become ideal MHD waves when the local Re^i and Re_m values are sufficiently high. The basic frequency and length scales for whistler waves are in the ranges of $\omega_{ci} \ll \omega \ll \omega_{ce}$ and $\lambda_e \ll L_0 \ll \lambda_i$.^{77,79} Therefore, whistler waves are a Hall-MHD phenomenon.

By linearizing the ideal MHD and Hall-MHD equations about the equilibrium and assuming plane wave solutions of the form $\exp(ik^*x^* - i\omega^*t^*)$, one obtains the Alfvén and whistler dispersion relations

$$\omega^* = k^* \quad \text{for Alfvén waves,} \quad (39)$$

$$(\omega^{*2} - k^{*2})^2 = \omega^{*2} k^{*4} \quad \text{for Whistler waves,} \quad (40)$$

where $k^* = 2\pi m/L_x^*$ is the wavenumber, m is the integer mode, and ω^* is the wave frequency. The initial conditions are

$$\begin{aligned} \rho_i^* &= 1, & u_i^* &= 0, & v_i^* &= -\delta^* \cos(k^*x^*), & w_i^* &= \delta^* \sin(k^*x^*), \\ p_i^* &= 1, & B_x^* &= 1, & B_y^* &= \delta^* v_p^* \cos(k^*x^*), & B_z^* &= -\delta^* v_p^* \sin(k^*x^*), \end{aligned}$$

where v_p^* is the phase velocity which can be calculated from linear Eqs. (39) and (40). The simulations are conducted over a periodic domain with a size of $L_x^* = 9.6$ and a number of grid points of $NX = 384$. Therefore, for the simulations conducted in this

study, the largest wave resolution is 192 points per wavelength for the minimum mode (i.e., $m = 2$). For the case using the maximum mode (i.e., $m = 30$), the wave resolution becomes 12.8 (= $384/30$) points per wavelength. The initial perturbation amplitude $\delta^* = 10^{-5}$ was used in all simulations.

Because Alfvén waves are believed to be the main mechanism for heating the solar corona,⁴ the characteristic number density, n_0 , length scale, L_0 , temperature, T_0 , and magnetic strength, B_0 , are chosen as the typical values for solar corona/flares.^{33,34} These characteristic values are $L_0 \sim 10^7\text{m}$, $n_0 \sim 10^{15}\text{m}^{-3}$, $T_0 = 100\text{eV}$, and $B_0 \sim 0.01\text{T}$, which leads to $\hat{\lambda}_i \sim 1.0 \times 10^{-6}$, $Re_m \sim 2.0 \times 10^{13}$, and $Re^i \sim 1.0 \times 10^4$. Figure 1(a) shows that the CFDNS results calculated using the two-fluid plasma equations in the global solar corona regime are in excellent agreement with the analytical linear stability theory (LST) predictions for ideal MHD over a wide range of modes, m .

The whistler waves found in solar corona/flares are related to the fast, collisionless magnetic reconnection that occurs on the length-scales comparable to the ion skin-depth.^{78,80} The ion-skin depth estimated using the typical parameter values of solar corona/flare parameters shown above is similar to the one provided in Ref. 34, i.e., $\lambda_i \approx 10\text{m}$. However, the viscous effects estimated using the closures described in Ref. 17 and Appendix A are probably not accurate at this scale, which is smaller than the mean free path for the solar corona/flares.^{33,34} Developing closures applicable to collisionless systems is difficult.⁸¹ Therefore, to be able to perform simulations relevant to the whistler wave dispersion relation, yet maintain the correspondence to the solar corona/flare parameters, we still use the above parameters, but decrease the reference temperature T_0 to obtain high enough values of $Re^i \approx 4.0 \times 10^3$ and $Re_m \approx 1.0 \times 10^4$. Again, as shown in Fig. 1(b), the CFDNS results calculated using the two-fluid plasma equations perfectly match the analytical solution given in Eq. (40).

B. Electromagnetic plasma shock

The presence of plasma shocks is also often observed in space and fusion applications. For example, the interaction of the solar wind with the Earth magnetosphere leads to the formation of a bow shock upstream of the magnetopause.^{82,83} The

electromagnetic plasma shock simulated here is an extension of the single-fluid, inviscid Brio-Wu shock⁸⁴ to the two-fluid plasma model. The initial values for the non-dimensional primary variables are

$$\begin{bmatrix} \rho_i^* \\ u_i^* \\ v_i^* \\ w_i^* \\ p_i^* \\ B_x^* \\ B_y^* \\ B_z^* \end{bmatrix} = \begin{bmatrix} 1.0 \\ 0.0 \\ 0.0 \\ 0.0 \\ 0.5 \\ 0.75 \\ 1.0 \\ 0.0 \end{bmatrix} \quad \text{For } x^* \leq 0.5 \quad \text{and}$$

$$\begin{bmatrix} \rho_i^* \\ u_i^* \\ v_i^* \\ w_i^* \\ p_i^* \\ B_x^* \\ B_y^* \\ B_z^* \end{bmatrix} = \begin{bmatrix} 0.125 \\ 0.0 \\ 0.0 \\ 0.0 \\ 0.05 \\ 0.75 \\ -1.0 \\ 0.0 \end{bmatrix} \quad \text{For } x^* > 0.5,$$

and Dirichlet boundary conditions are implemented at the shock-tube boundaries.

Most (if not all) previous numerical studies of the bow shock^{48,51,85} and Brio-Wu shock^{61,84,86} ignore the viscous and heat flux terms and fully rely on the numerical dissipation introduced by shock-capturing schemes to regularize the equations around sharp discontinuities. In contrast, by including full plasma transport terms, one should be able to resolve the shocks by using high-order non-dissipative numerical schemes at a sufficiently high grid resolution. Therefore, in this test case, we choose the characteristic number density, $n_0 \sim 10^7\text{m}^{-3}$, length scale, $L_0 \sim 10^{11}\text{m}$, and magnetic strength, $B_0 \sim 10\text{nT}$, as the typical values found in solar wind,^{51,79,85} and vary T_0 to obtain

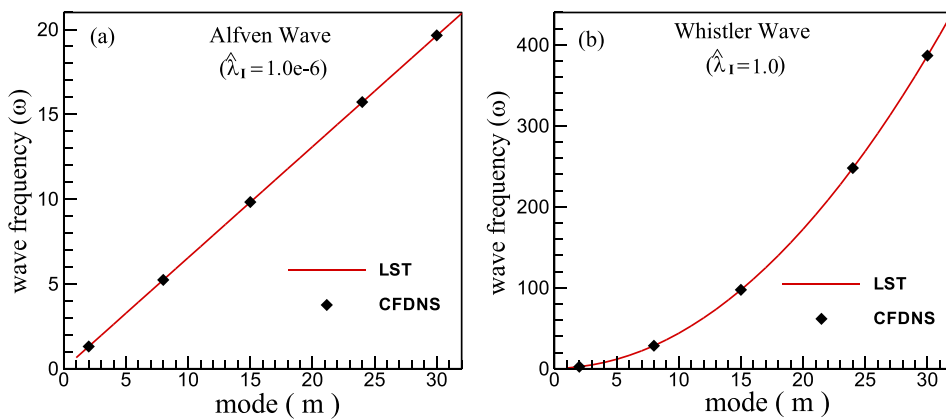


FIG. 1. Comparison of analytical Alfvén and whistler dispersion relations (LST) with numerical solutions calculated by using the two-fluid plasma solver (CFDNS) in (a) ideal MHD regime and (b) Hall-MHD regime.

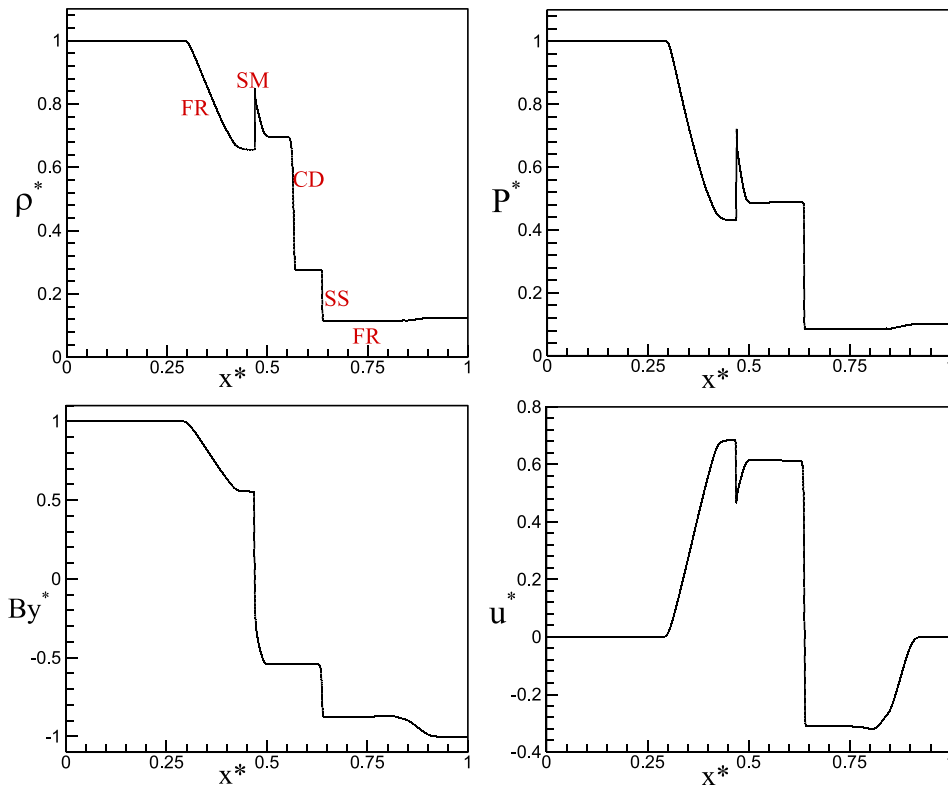


FIG. 2. CFDNS results calculated by using two-fluid plasma equations for plasma shock with the normalized ion skin depth, $\hat{\lambda}_i = 1.0 \times 10^{-6}$, the magnetic Reynolds number, $Re_m \sim 1.0 \times 10^{12}$, and the ion viscous Reynolds number, $Re^i = 6.3 \times 10^3$.

a range of substantial high, but still affordable Reynolds numbers. These reference scales give $\hat{\lambda}_i \sim 1.0 \times 10^{-6}$ and $Re_m \sim 10^{12}$, and therefore, both the Hall effect and the magnetic resistivity become negligible.

Figure 2 shows that, without the need to explicitly turn off the corresponding terms from the governing equations, the ideal MHD results including the slow compound wave (SM), contact discontinuity (CD), and slow shock (SS) are obtained from the two-fluid plasma solver for flows with large enough Reynolds numbers. In the presence of physical viscosity, the shock wave is no longer zero-thickness. Instead, the value of the shock thickness depends on the local Reynolds number. Therefore, all shock structures can be fully

resolved by using high-order non-dissipative numerical schemes, provided that the grid resolutions are sufficiently high. Of course, by increasing viscosity or decreasing the Reynolds number, the profiles for all variables become smoother and, therefore, can easily be resolved at lower grid resolutions.

In this study, grid convergence tests have been conducted for all plasma shock cases to guarantee that computational results presented are free of numerical error. As indicated in Fig. 3, fully resolved DNS-like solutions are obtained at all ion viscous Reynolds numbers when the ion grid Reynolds number, $Re_\Delta = Re^i/NX$, is smaller than a threshold value, which is 2.3 for our 6th order compact finite difference solver.

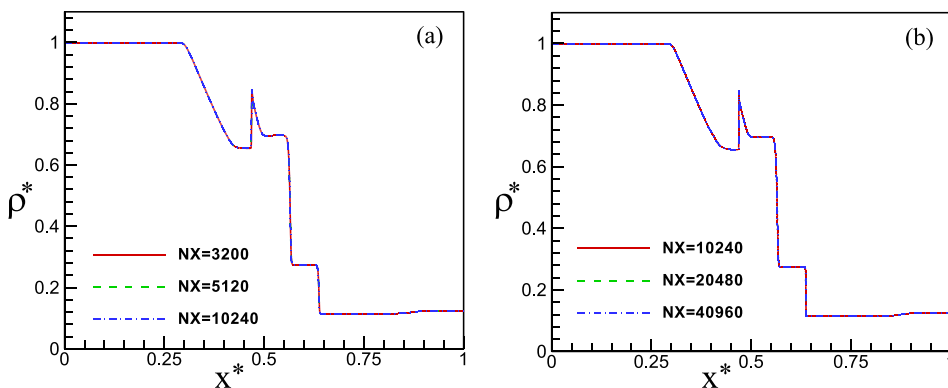


FIG. 3. Fully converged CFDNS results for plasma shocks at two ion viscous Reynolds numbers (a) $Re^i = 6.3 \times 10^3$ and (b) $Re^i = 2.3 \times 10^4$.

By using the finest grid solutions as the exact results, i.e., $NX = 40960$ for $Re^i = 6.3 \times 10^3$ and $NX = 122880$ for $Re^i = 2.3 \times 10^4$, Fig. 4 shows that the grid convergence rates are $\hat{n} = 6.14$ for the $Re^i = 6.3 \times 10^3$ case and $\hat{n} = 6.08$ for $Re^i = 2.3 \times 10^4$ cases. Both values are very close to the theoretical limit of the sixth-order compact finite difference scheme. This shows that the high-order two-fluid plasma solver results are free of the spurious behavior commonly found in high-order shock-capturing scheme results, like the modification of the discontinuity location.⁸⁷ Second, the CFDNS results maintain nearly 6-order accuracy across the discontinuities, while the convergence rate of most shock-capturing schemes drops to first-order accuracy near discontinuities.⁸⁸

C. Magnetic reconnection

The last test case considered in this study is the collisionless magnetic reconnection, a rapid rearrangement of magnetic field topology, and release of free magnetic energy. It is of particular importance to the dynamic evolution of the solar corona/flares,^{4,78} the magnetosphere,^{89,90} and thermonuclear fusion.^{91,92} Previous studies^{6,43,44,53,80} confirm that the fast magnetic reconnection occurs on a length scale comparable to the ion skin depth and is mainly contributed by the Hall term.

Although extensive computational work has been done on the magnetic reconnection problem, simulations of magnetic reconnection with explicit viscous and thermal diffusion effects are rare. In addition, instead of a dynamically changing property, the resistivity in most previous studies^{43,56} was simply chosen as a constant value. The justification for the absence of physical plasma transport terms is partially because the rapid magnetic reconnection is collisionless, therefore, the closures for transport terms based on Chapman-Enskog expansion in the small mean-free-path¹⁷ become inappropriate, while developing closures applicable to collisionless systems is difficult.⁸¹ In turn, most widely used plasma solvers use dissipative shock-capturing techniques and rely on numerical dissipation instead of physical transport terms to regularize the equations. In general, in such approaches, the numerical dissipation is related to the mesh size and the simulations do not converge as the mesh size is increased. Therefore, it seems impossible for such plasma flow solvers to produce fully resolved DNS-like solutions.

In this study, we choose the characteristic number density and length scale as the typical values found in solar flare reconnection,³⁴ i.e., $L_0 \sim 10\text{m}$ and $n_0 \sim 10^{15}\text{m}^{-3}$, which leads to $\lambda_i = 1.0$. We demonstrate that physical transport can be used to obtain mesh converged solutions with negligible numerical dissipation. Moreover, as the viscous Reynolds number is increased, the solutions tend to converge and predict the collisionless magnetic reconnection results. We vary the reference temperature, T_0 , and magnetic strength, B_0 , to generate a wide range of viscous Reynolds number, Re^i , and magnetic Reynolds number, Re_m , values. The range of Re_m values is chosen to include values used in previous studies, i.e., $Re_m = 100 - 350$ and $Re_m = 200$ employed by Ma and Bhattacharjee⁴³ and Toth et al.,⁵⁶ respectively.

Similar to previous studies, the initial conditions for the non-dimensional primary variables are

$$\begin{bmatrix} \rho_i^* \\ u_i^* \\ v_i^* \\ w_i^* \\ p_i^* \\ B_x^* \\ B_y^* \\ B_z^* \end{bmatrix} = \begin{bmatrix} 1/5 + \text{sech}^2(2x^*) \\ 0.0 \\ 0.0 \\ 0.0 \\ [1/5 + \text{sech}^2(2x^*)]/4 \\ (2\pi/10L_y^*) \times \sin(2\pi y^*/L_y^*) \times \cos(\pi x^*/L_x^*) \\ \tanh(2x^*) - (\pi/10L_x^*) \times \cos(2\pi y^*/L_y^*) \times \sin(\pi x^*/L_x^*) \\ 0.0 \end{bmatrix}.$$

The perfectly conducting wall boundary condition is applied in the vertical direction (x^*) and the periodic boundary condition is implemented in the horizontal direction (y^*). The simulations are conducted in a two-dimensional domain with $L_x^* = 12.8$ and $L_y^* = 25.6$.

Figures 5 and 6 show that the two-fluid non-dissipative plasma solver (i.e., CFDNS) with temperature and magnetic field dependent transport (ion/electron viscous stress, heat flux, frictional drag force, and magnetic resistivity) can successfully reveal the whole magnetic reconnection process. For example, Fig. 5 shows that, during the reconnection process, the high-density sheet is stretched and finally broken up into two ligaments, which further shrink to increase the high density values. In contrast to

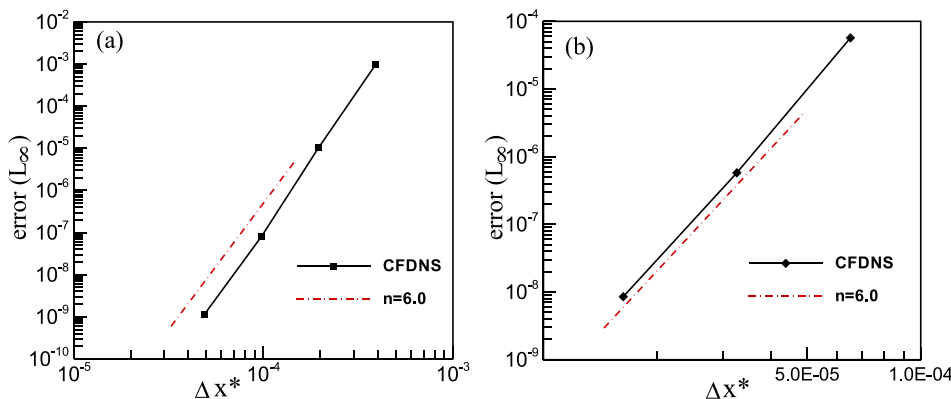


FIG. 4. The comparison of grid convergence rates calculated by two-fluid plasma solver for plasma shock at two ion viscous Reynolds numbers (a) $Re^i = 6.3 \times 10^3$ and (b) $Re^i = 2.3 \times 10^4$ with the theoretical limit of the sixth-order compact scheme ($n = 6$).

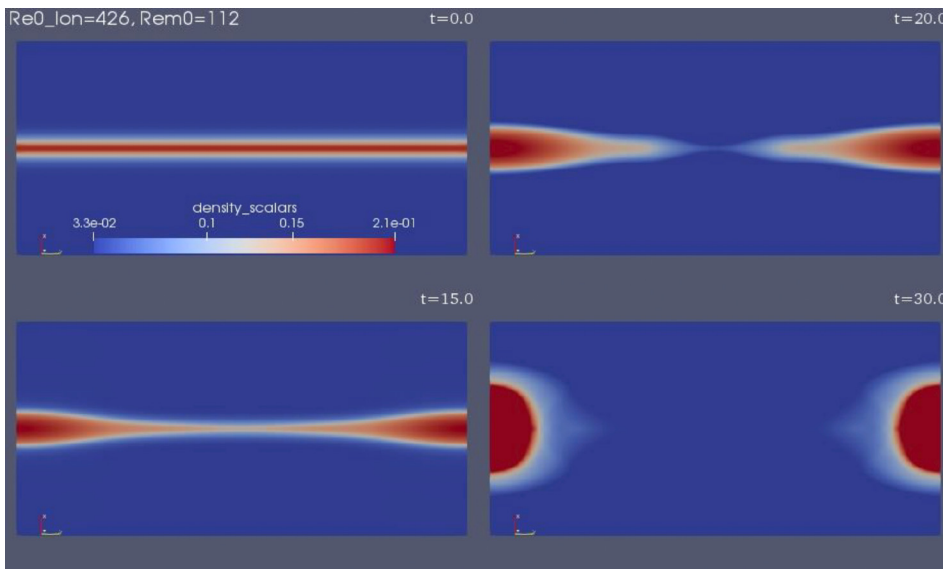


FIG. 5. The temporal variation of density contours during magnetic reconnection with $Re_m \approx 112$ and $Re^l \approx 426$.

previous two-fluid plasma results without transport terms,⁵⁷ the CFDNS results remain perfectly symmetric, which indicates the high accuracy of the two-fluid plasma solver in handling this challenging plasma flow. Figure 6 clearly shows that, as the reconnection takes place, the magnetic streamlines tend to bend from the horizontal direction to the vertical direction and the intensity of the vertical component, B_x , increases dramatically. This corresponds to a rapid increase in reconnection flux and an eruptive release of magnetically stored energy to heat the plasma.

The temperature contours shown in Fig. 7 further confirm the rapid conversion of magnetic energy into particle energy. As the reconnection takes place, both temperature and velocities (not shown) increase significantly due to the rapid conversion of magnetic energy into thermal and kinetic energies. In the solar corona, this phenomenon is thought to give rise to solar flares and drive the outflow of the solar wind.⁴ Consistently, the rapid increase in

temperature causes a dramatic increase in heat flux and viscous dissipation, since $\kappa \propto T^{5/2}$ and $\mu^s \propto T^{5/2}$, as well as a large decrease in magnetic resistivity, since $\eta \propto T^{-3/2}$. The presence of thermal diffusion is then absolutely necessary to prevent unphysically high temperatures to be generated at the reconnection points. Previous studies without physical thermal diffusion had to rely on the numerical diffusion introduced by dissipative numerical schemes to damp this effect. The effect of numerical diffusion is hard to quantify due to the higher order nonlinearities usually present in the associated terms (if such terms can be explicitly evaluated at all). In addition, different numerical schemes have different truncation errors, and so, numerical diffusion is difficult to generalize across various codes. Thus, numerical results relying on numerical diffusion to regularize the equations should be regarded with caution.

A grid convergence test has been conducted for the magnetic reconnection problem, and the reconnection fluxes

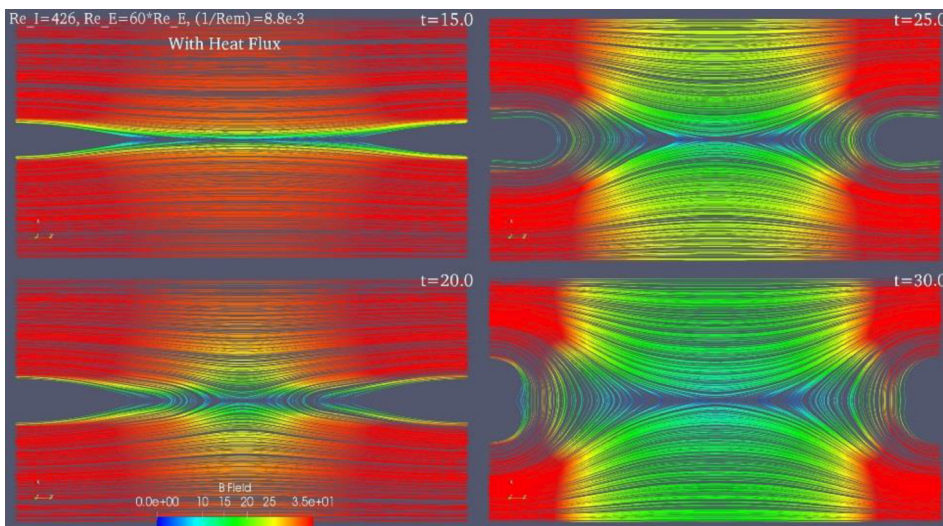


FIG. 6. The temporal variation of magnetic streamlines during magnetic reconnection with $Re_m \approx 112$ and $Re^l \approx 426$.

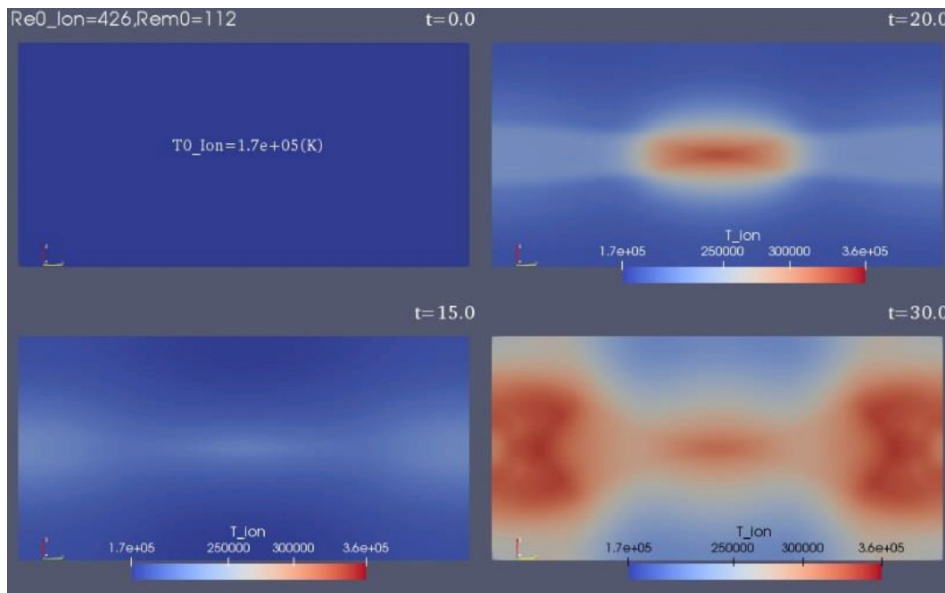


FIG. 7. The temporal variation of ion temperature contours during magnetic reconnection with $Re_m \approx 112$ and $Re^i \approx 426$.

calculated using the two-fluid plasma solver are converged at a moderate grid resolution (e.g., 256×512) for $Re^i = 426$ and $Re_m = 112$, as shown in Fig. 8(a). By using the finest grid (e.g., 768×1536) results as the exact solutions, one can calculate the numerical error on coarser grids. The results are shown in Fig. 8(b). The grid convergence rate estimated from the last two points is $\hat{n} = 6.58$, which is fairly close to the theoretical limit of the sixth-order compact scheme. Fully converged DNS-like results can also be observed in cases with higher viscous Reynolds number, provided that the grid resolution is sufficiently large. For example, the CFDNS results for the case with initial ion Reynolds number $Re^i = 850$ are fully converged at a grid resolution of 384×768 . In this test case, the threshold value for fully converged DNS-like results is around $Re_\Delta \approx 2.6$. In addition to the reconnection flux profile, the 2D contours of vertical velocity and spanwise current density shown in Fig. 9 further confirm that the CFDNS results presented here are indeed fully converged DNS-like solutions.

Finally, to examine the effects of the plasma transport terms and convergence of the results with the Reynolds number,

we have conducted a series of simulations for a range of Re^i and Re_m values. First, as observed in Fig. 10(a), viscosity has a slight delay effect on the reconnection time, as Re^i is increased from 124 to 850. However, for all viscous Reynolds numbers, Re^i , the magnetic flux saturates to the same non-dimensional value of around 4.0 at a non-dimensional time close to 40.0. These values are consistent with those reported in Refs. 6 and 43. In addition, the time variations of the reconnection flux quickly converge at Re^i values above ~ 400 . For $Re^i = 426$, Fig. 10(b) shows that the magnetic flux also converges as the magnetic Reynolds number is increased to $Re_m = 890$.

Based on this convergence, we assess that the results obtained with $Re^i = 426$ and $Re_m = 890$ fully represent the collisionless reconnection process for the number density and length scale shown above, representative of solar flare reconnection. In addition, due to the robustness of the saturation flux value and time to the viscosity value, the results are also very similar to numerical results relying on numerical dissipation for regularization. On the other hand, resistivity has a larger effect than viscosity at moderate Re_m values [Fig. 10(b)], in particular

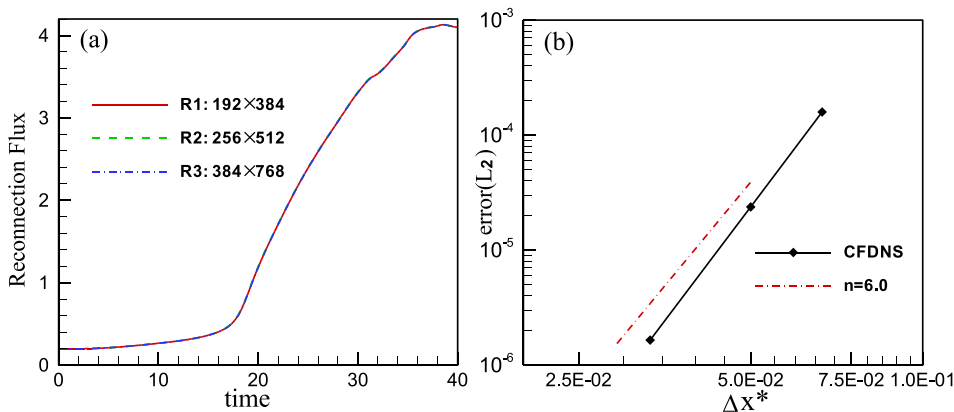


FIG. 8. (a) Temporal variation of reconnection flux at different resolutions and (b) comparison of the grid convergence rate for the two-fluid plasma solver results ($\hat{n} = 6.58$) against the theoretical limit of the sixth-order compact finite difference scheme. The simulations were conducted with $Re_m \approx 112$ and $Re^i \approx 426$.

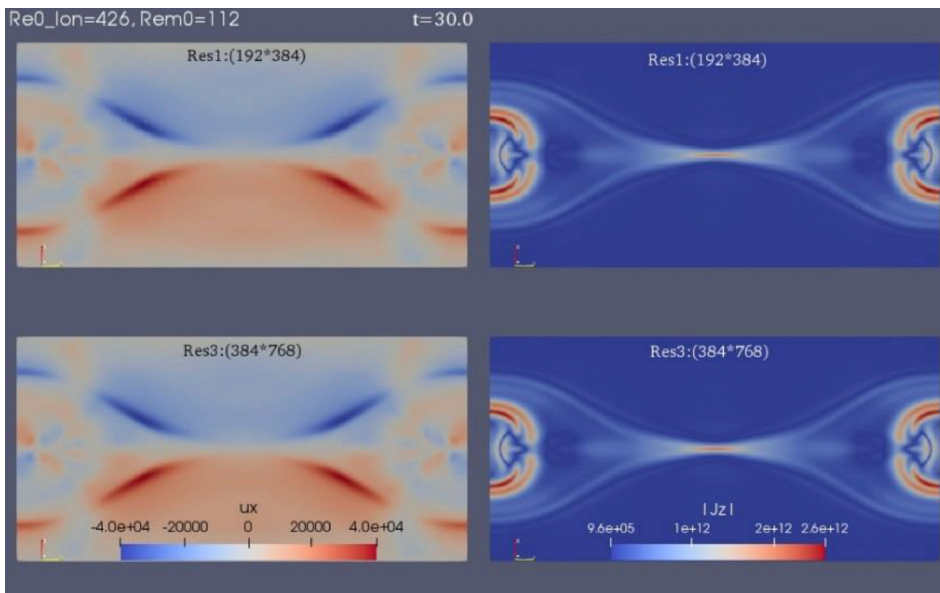


FIG. 9. The contours of vertical velocity, V_x , and spanwise current density, $|J_z|$, with different resolutions for $Re_m \approx 112$ and $Re^i \approx 426$.

on the reconnection time. Lower resistivity or large Re_m values lead to an earlier reconnection and slightly larger saturation flux values. The reconnection time and saturation flux value for the case $Re_m = 224$ shown in Fig. 10(b) are very close to those predicted by previous Hall-MHD simulations⁵⁶ with $Re_m = 200$. However, due to the larger potential effect of the numerical regularization scheme regarding resistivity, predictions using the ideal (inviscid and perfect conductivity) two-fluid plasma model (e.g., Ref. 45), need to be evaluated with more caution. Nevertheless, again, the convergence of the results, as Re^i and Re_m are increased, explains why previous studies using relatively low Re_m values are still useful in predicting the magnetic reconnection phenomena occurring in space.

V. CONCLUSION

In this study, to be able to generate high-order fully converged DNS-like solutions for plasma flow problems, we have implemented the Braginskii two-fluid plasma model with full plasma transport terms, including temperature and magnetic

field dependent ion and electron viscous stresses and heat fluxes, frictional drag force, and ohmic heating term, in the CFDNS code, using sixth-order non-dissipative compact finite differences with negligible numerical dissipation/diffusion. To maintain computational feasibility, while also solving all the dynamically relevant time and length scales, the infinite speed of light and negligible electron inertia assumptions have been used.

The range of applicability of the resulting two-fluid plasma equations was discussed in detail. This was achieved by using a non-dimensional analysis of the equations, which highlights the relevant non-dimensional parameters. These parameters are cast in terms of characteristic scales found in practical problems of interest, including the characteristic number density, n_0 , length scale L_0 , temperature, T_0 , and magnetic strength, B_0 . The non-dimensional parameters can be used to estimate the relative contributions of Hall and Biermann battery effects, resistivity, viscous stress, and heat flux in different regimes. In the appropriate limits, the two-fluid plasma equations recover the conventional MHD (i.e., ideal, resistive, and Hall) equations. First,

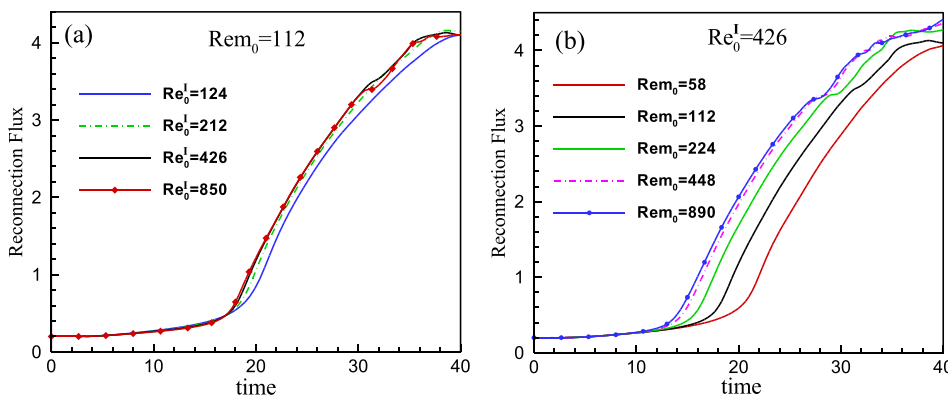


FIG. 10. The temporal variations of reconnection flux for different viscosities and magnetic resistivities.

the corresponding non-dimensional single fluid equations for the mixture velocity, density, pressure, and temperature are derived. Then, (i) conventional Hall-MHD equations can be recovered in regimes where $0 \ll \hat{\lambda}_i \ll \sqrt{m_i/m_e}$ (and/or $0 \ll \hat{r}_{Li} \ll \sqrt{m_i/m_e}$), $Re^i, Re^e \rightarrow \infty$, and $Fr \rightarrow \infty$; (ii) Resistive MHD equations can be recovered in regimes where $\hat{\lambda}_i \rightarrow 0$ (and/or $\hat{r}_{Li} \rightarrow 0$), $Fr \rightarrow \infty$, and $Re^i, Re^e \rightarrow \infty$, but Re_m has a finite value; and (iii) Ideal MHD equations are recovered in regimes when in addition $Re_m \rightarrow \infty$. The single fluid and the conventional Hall-MHD equations are unclosed due to the explicit presence of the electron pressure. Several choices for closing these equations in previous studies are discussed. In contrast, the two-fluid plasma equations are more general and do not need additional assumptions.

The two-fluid solver was demonstrated against four canonical problems, to confirm its accuracy and robustness in handling plasma flows in different regimes. These test cases include the Alfvén and whistler waves for parameter values relevant to solar corona, the electromagnetic Brio-Wu plasma shock⁸⁴ with parameter values relevant to the bow shock caused by the interaction between solar wind and the earth magnetosphere, and the fast magnetic reconnection in solar flares. All physical transport terms are retained for the four test cases, and the convergence with respect to the viscous and magnetic Reynolds numbers was discussed, in addition to proving grid convergence of the results. For both Alfvén and whistler dispersion relations, the numerical results are in excellent agreement with the analytical or linear stability theory (LST) predictions for the corresponding ideal MHD and Hall-MHD equations over a wide range of wavenumbers. Because of the inclusion of physical viscosity in the two-fluid plasma solver, all plasma shock characteristics can be fully resolved at all Reynolds numbers, provided that the grid resolution is sufficiently high. This means that the ion grid Reynolds number, $Re_\Delta = Re^i/NX$, needs to be smaller than a threshold value, which for the plasma shock test case is around 2.3. Near the sharp gradients in the plasma shock problem, in contrast to the first-order convergence rate commonly found in studies using shock-capturing schemes, the grid convergence rate calculated here is in the range of $\hat{n} \sim 6.08 - 6.14$ which is very close to the theoretical value of the sixth-order compact scheme.

For the last test case, the CFDNS results successfully demonstrate, using the two-fluid plasma model, the fast magnetic reconnection process occurring under solar flare conditions. The magnetic flux saturation time and value predicted here are in good agreement with those reported in previous studies under similar conditions. The systematic examination of Re^i and Re_m effects on the magnetic reconnection reveals that the results are converged for the largest values used in this study, $Re^i = 426$ and $Re_m = 890$. This implies that the results are relevant to practical problems with much larger Reynolds numbers. The viscous effects are relatively small for $Re^i \sim 100 - 400$, so that coarse resolution simulation results using numerical dissipation to regularize the equations are likely close to the high Reynolds number results. On the other hand, the reconnection flux saturation value and time are more sensitive to changes in Re_m . The CFDNS results with $Re_m \sim 200$ are close to those reported in previous studies, but

the results become converged at much higher magnetic Reynolds number values ($Re_m > 800$). These results are particularly useful in evaluating the different approximations used in plasma solvers (e.g., with/without viscosity, heat flux, resistivity, etc.).

In general, the Braginskii transport coefficients become inaccurate for degenerate and/or partially ionized plasmas. However, more general formulations do not include the full directional dependence of the physical transport with respect to the magnetic field or are less accurate for low-Z materials. Future simulations will address the importance of anisotropic transport and differences with more accurate models where available (e.g., for higher-Z materials) and further explore the existence of a mixing transition in various applications.

ACKNOWLEDGMENTS

This work was made possible in part by funding from the LDRD program at the Los Alamos National Laboratory through Project No. 20150568ER. Z. Li was supported by the Los Alamos National Laboratory, under Grant No. 430461. The Los Alamos National Laboratory is operated by Triad National Security, LLC, for the National Nuclear Security Administration of U.S. Department of Energy (Contract No. 89233218CNA000001). Computational resources were provided by the Los Alamos National Laboratory Institutional Computing Program and the High Performance Computing Center at Texas A&M University-Corpus Christi.

APPENDIX A: PLASMA TRANSPORT TERM FORMULATIONS

For completeness, the formulations for all transport terms, mostly following Ref. 17, as well as the details of their implementation are given below.

1. Viscous stress tensors, π_s

In general, three major steps are needed for calculating the viscous stress. First, the strain rate tensor, \mathbf{W}_s , is calculated in the fixed Cartesian coordinate system, $\{\mathbf{e}_1, \mathbf{e}_2, \mathbf{e}_3\}$, as follows:

$$\mathbf{W}_s = - \left[\nabla \mathbf{u}_s + (\nabla \mathbf{u}_s)^T - \frac{2}{3} (\nabla \cdot \mathbf{u}_s) \mathbf{I} \right], \quad (A1)$$

where \mathbf{I} is the second-order identity tensor.

The next step is to restate the strain rate tensor, \mathbf{W}_s , into a moving coordinate system aligned with the magnetic field, $\{\mathbf{e}'_1, \mathbf{e}'_2, \mathbf{e}'_3\}$, in which $\mathbf{e}'_3 = \mathbf{B}/|\mathbf{B}|$ denotes the unity vector in the direction of the magnetic field, as follows:

$$\mathbf{W}'_s = \mathbf{Q}^T \mathbf{W}_s \mathbf{Q}. \quad (A2)$$

The transformation matrix, \mathbf{Q} , is defined by

$$\mathbf{Q} = \begin{bmatrix} -B'_2 & -B'_1 B''_3 & B'_1 \\ B'_1 & -B'_2 B''_3 & B'_2 \\ 0 & B'_1 B''_1 + B'_2 B''_2 & B'_3 \end{bmatrix}, \quad (A3)$$

where $B'_i = B_i/\sqrt{B_1^2 + B_2^2}$ and $B''_i = B_i/\sqrt{B_1^2 + B_2^2 + B_3^2}$. The viscous stress in the new coordinate system can then be calculated as

$$\pi'_{11,s} = -\frac{1}{2}\mu_0^s(W'_{11,s} + W'_{22,s}) - \frac{1}{2}\mu_1^s(W'_{11,s} - W'_{22,s}) - \mu_3^s W'_{12,s}, \quad (\text{A4})$$

$$\pi'_{12,s} = \pi'_{21,s} = -\mu_1^s W'_{12,s} + \frac{1}{2}\mu_3^s(W'_{11,s} - W'_{22,s}), \quad (\text{A5})$$

$$\pi'_{13,s} = \pi'_{31,s} = -\mu_2^s W'_{13,s} - \mu_4^s W'_{23,s}, \quad (\text{A6})$$

$$\pi'_{22,s} = -\frac{1}{2}\mu_0^s(W'_{11,s} + W'_{22,s}) - \frac{1}{2}\mu_1^s(W'_{22,s} - W'_{11,s}) + \mu_3^s W'_{12,s}, \quad (\text{A7})$$

$$\pi'_{23,s} = \pi'_{32,s} = -\mu_2^s W'_{23,s} + \mu_4^s W'_{13,s}, \quad (\text{A8})$$

$$\pi'_{33,s} = -\mu_0^s W'_{33,s}, \quad (\text{A9})$$

where μ_j^s , $j = 1, \dots, 4$ are the ion and electron viscosity coefficients which are mainly functions of temperature, T_s , and number density, n_s . For ions, one has $\mu_0^i = (2.23/2.33)n_i k_B T_i \tau_i$, $\mu_2^i = n_i k_B T_i \tau_i (1.2x^2 + 2.23)/\Delta$, and $\mu_4^i = n_i k_B T_i \tau_i x (x^2 + 2.38)/\Delta$, where $x = \omega_{ci} \tau_i$ and $\Delta = x^4 + 4.03x^2 + 2.33$. The coefficients μ_1^i and μ_3^i can be obtained by replacing x by $2x$ in the formulations for μ_2^i and μ_4^i , respectively. Here, $\tau_i = 12\pi^{3/2} e_0^2 \sqrt{m_i} (k_B T_i)^{3/2} / (\ln \Lambda e^4 Z^4 n_i)$ is the ion collision time and $\omega_{ci} = Ze|\mathbf{B}|/m_i$ is the ion cyclotron frequency. For electrons, one has $\mu_0^e = (8.50/11.6)n_e k_B T_e \tau_e$, $\mu_2^e = n_e k_B T_e \tau_e (2.05x^2 + 8.50)/\Delta$, and $\mu_4^e = -n_e k_B T_e \tau_e x (x^2 + 7.91)/\Delta$, where $x = \omega_{ce} \tau_e$ and $\Delta = x^4 + 13.8x^2 + 11.6$. Similarly, the coefficients μ_1^e and μ_3^e can be obtained by replacing x by $2x$ in the formulations for μ_2^e and μ_4^e , respectively. Here, $\tau_e = 6\sqrt{2}\pi^{3/2} e_0^2 \sqrt{m_e} (k_B T_e)^{3/2} / (\ln \Lambda e^4 Z n_e)$ is the electron collision time and $\omega_{ce} = e|\mathbf{B}|/m_e$ is the electron cyclotron frequency.

In this study, the Coulomb logarithm formula, $\ln \Lambda$, is adopted from Ref. 93 and its expression in Gaussian units is given as follows:

$$\ln \Lambda = \begin{cases} -\ln \left(\sum_{k=1}^5 a_k g^k \right), & \text{if } g = (Ze)^2 / k_B \lambda_{eff} T_e \leq 1 \\ 2 \times \frac{b_0 + b_1 \ln(g) + b_2 \ln^2(g)}{1 + b_3 g + b_4 g^2}, & \text{if } g = (Ze)^2 / k_B \lambda_{eff} T_e > 1. \end{cases} \quad (\text{A10})$$

The numerical values of the constant coefficients $a_1, a_2, \dots, a_5, b_0, \dots, b_4$ can be found in Ref. 93. The effective screening length λ_{eff} can be estimated as

$$\lambda_{eff} = \lambda_e \left(1 + \frac{1}{1 + 3\Gamma} \right)^{-1/2}, \quad (\text{A11})$$

where $\lambda_e = [k_B T_e / (4\pi Z^2 e^2 n_e)]^{1/2}$, $\Gamma = (Ze)^2 / \hat{a}_i k_B T_e$, and $\hat{a}_i = (3/4\pi n_e)^{1/3}$.

Finally, the viscous stress tensor, π_s , can be obtained by restating π'_s back into the fixed coordinate system, $\{\mathbf{e}_1, \mathbf{e}_2, \mathbf{e}_3\}$, as follows:

$$\pi_s = \mathbf{Q} \pi'_s \mathbf{Q}^T. \quad (\text{A12})$$

For the special case without the magnetic field, i.e., $\mathbf{B} = 0$, the viscous stress tensor can be calculated directly by using the following formulation:

$$\pi_s = \mu_0^s \mathbf{W}_s. \quad (\text{A13})$$

Another special situation is when the magnetic field is aligned with the fixed coordinate system, i.e., $B_1 = B_2 = 0$ and $B_3 \neq 0$. In this case, the transformation matrix, \mathbf{Q} , is reduced to the second-order identity tensor \mathbf{I} . Therefore, no coordinate transformation is needed and the viscous stress tensor can be calculated by using Eqs. (A4)–(A9) directly.

2. Heat flux, \mathbf{q}_s

The ion heat flux, \mathbf{q}_i , is caused by the temperature gradient only and can be expressed as

$$\mathbf{q}_i = -\left(\frac{n_i k_B^2 T_i \tau_i}{m_i} \right) \left[\eta_0 \nabla_{\parallel} T_i + \left(\frac{\eta'_1 x^2 + \eta'_0}{\Delta} \right) \nabla_{\perp} T_i - \frac{x(\eta''_1 x^2 + \eta''_0)}{\Delta} (\mathbf{h} \times \nabla T_i) \right], \quad (\text{A14})$$

where $\mathbf{h} = \mathbf{B}/|\mathbf{B}|$ represents a unity vector in the direction of the local magnetic field and the symbols \parallel and \perp on any vector denote its component in the parallel or perpendicular direction to the magnetic field, \mathbf{B} , respectively. For example, $\nabla_{\parallel} T_i = \mathbf{h}(\mathbf{h} \cdot \nabla T_i)$ and $\nabla_{\perp} T_i = \mathbf{h} \times (\nabla T_i \times \mathbf{h}) = \nabla T_i - \nabla_{\parallel} T_i$. The non-dimensional variables x and Δ follow the above definitions.

In contrast, the electron heat flux, \mathbf{q}_e , is caused by both the temperature gradient and the relative velocity between ions and electrons, $(\mathbf{u}_i - \mathbf{u}_e)$ or current density, \mathbf{J} , and can be written as $\mathbf{q}_e = \mathbf{q}_{Te} + \mathbf{q}_{ue}$. The two parts are formulated as

$$\mathbf{q}_{Te} = -\left(\frac{n_e k_B^2 T_e \tau_e}{m_e} \right) \left[\gamma_0 \nabla_{\parallel} T_e + \left(\frac{\gamma'_1 x^2 + \gamma'_0}{\Delta} \right) \nabla_{\perp} T_e - \frac{x(\gamma''_1 x^2 + \gamma''_0)}{\Delta} (\mathbf{h} \times \nabla T_e) \right], \quad (\text{A15})$$

$$\mathbf{q}_{ue} = -\frac{k_B T_e}{e} \left[\beta_0 \mathbf{J}_{\parallel} + \left(\frac{\beta'_1 x^2 + \beta'_0}{\Delta} \right) \mathbf{J}_{\perp} + \frac{x(\beta''_1 x^2 + \beta''_0)}{\Delta} (\mathbf{h} \times \mathbf{J}) \right]. \quad (\text{A16})$$

The numerical values of the constant coefficients, $\eta_0, \gamma_0, \beta_0, \gamma'_0$, etc., can be found in Ref. 17.

3. Frictional drag force, \mathbf{R}_s

Similar to the electron heat flux, \mathbf{q}_e , the frictional drag force between ions and electrons, \mathbf{R}_{ei} (or \mathbf{R}_e), also has two different contributions

$$\mathbf{R}_u = \left(\frac{m_e}{e \tau_e} \right) \left[\alpha_0 \mathbf{J}_{\parallel} + \left(1 - \frac{\alpha'_1 x^2 + \alpha'_0}{\Delta} \right) \mathbf{J}_{\perp} - \frac{x(\alpha''_1 x^2 + \alpha''_0)}{\Delta} (\mathbf{h} \times \mathbf{J}) \right], \quad (\text{A17})$$

$$\mathbf{R}_T = -(n_e k_B) \left[\beta_0 \nabla_{\parallel} T_e + \left(\frac{\beta'_1 x^2 + \beta'_0}{\Delta} \right) \nabla_{\perp} T_e + \frac{x(\beta''_1 x^2 + \beta''_0)}{\Delta} (\mathbf{h} \times \nabla T_e) \right]. \quad (\text{A18})$$

\mathbf{R}_u is the classical momentum frictional force caused by the velocity difference between ions and electrons, while the thermal frictional force, \mathbf{R}_T , is produced by the electron temperature gradient.

4. Collision generated heat, Q_s

Following the approximations made in Refs. 17 and 54, the ion and electron collision generated heat terms are written as

$$Q_i = Q_\Delta = 3 \left(\frac{m_e}{m_i} \right) \left(\frac{n_e}{\tau_e} \right) k_B (T_e - T_i), \quad (\text{A19})$$

$$Q_e = \mathbf{R}_e \cdot (\mathbf{u}_i - \mathbf{u}_e) - Q_\Delta. \quad (\text{A20})$$

The expression $\mathbf{R}_u \cdot (\mathbf{u}_i - \mathbf{u}_e)$ is the general ohmic heating term.

We note here that the Braginskii coefficients are consistently derived using two-term Sonine polynomial solutions. The electron conductivity model presented in Ref. 68 reduces to the Braginskii model for fully ionized nondegenerate plasmas but retains a higher precision for the numerical coefficients due a different treatment of the Sonine polynomial solution. Thus, most of the coefficients appearing in the heat flux and frictional drag force Braginskii formulas are about 8% different from the exact values. On the other hand, Ref. 68 does not include electron-electron scattering, which adds a non-negligible contribution for low-Z materials, where the model overestimates the conductivity. For consistency with the other transport formulas and to consider the full directional dependence of the transport, here, we use the Braginskii formulation for the heat flux and frictional drag force and will address the differences compared to the formulation in Ref. 68 elsewhere.

APPENDIX B: QUASI-NEUTRALITY CONDITION

As discussed in Sec. IID, an indication of the accuracy of the numerical integration is that the charge density, ρ_c , evaluated from the divergence of the electric field, \mathbf{E} , remains sufficiently small at all the times. For all test cases discussed in

this paper, the maximum normalized charge density in the computational domain, $|\bar{\rho}_c|_{\max} = |\epsilon_0 \nabla \cdot \mathbf{E} / (eZn_i)|_{\max}$, was monitored throughout the simulation times.

Figure 11 shows $|\bar{\rho}_c|_{\max}$ variation for the 1D plasma shock and 2D magnetic reconnection problems. Both cases exhibit sufficiently small values to conclude that the simulations conducted in this study satisfy the quasi-neutrality condition.

APPENDIX C: SINGLE-FLUID LIMITING EQUATIONS

The single-fluid plasma equations (35)–(38) described in Sec. IIIB are derived from the non-dimensional two-fluid plasma equations (20)–(27) by using the ion-electron mixture definitions, infinite speed of light, and negligible electron inertia assumptions. The Hall term, electron pressure term, and all plasma transport terms are retained in the single-fluid plasma equations, which can be viewed as full Hall-MHD equations, in contrast to the conventional Hall-MHD equations where the viscous, heat flux, and acceleration terms are neglected. As shown in this Appendix, the conventional Hall, resistive, and ideal MHD equations can be recovered from the general single-fluid equations (35)–(38) as limiting cases.

1. The conventional Hall-MHD equations

In regimes where $Re^i, Re^e \rightarrow \infty$, $\mathbf{q}_{ue}^* \rightarrow 0$, and $\mathbf{R}_T^* \rightarrow 0$ and assuming that the gradients remain finite, the single-fluid equations (35)–(38) given in Sec. IIIB reduce to

$$\frac{\partial \rho^*}{\partial t^*} + \nabla^* \cdot (\rho^* \mathbf{u}^*) = 0, \quad (\text{C1})$$

$$\frac{\partial (\rho^* \mathbf{u}^*)}{\partial t^*} + \nabla^* \cdot (\rho^* \mathbf{u}^* \mathbf{u}^*) = -\beta \nabla^* p^* + \mathbf{J}^* \times \mathbf{B}^*, \quad (\text{C2})$$

$$\frac{1}{\gamma - 1} \left[\frac{\partial p^*}{\partial t^*} + \nabla^* \cdot (p^* \mathbf{u}^*) \right] = -p^* \nabla^* \cdot \mathbf{u}^* + \frac{\hat{\lambda}_i}{\gamma - 1} \nabla^* \cdot \left(\frac{p_e^* \mathbf{J}^*}{\rho^*} \right) + \hat{\lambda}_i p_e^* \nabla^* \cdot \left(\frac{\mathbf{J}^*}{\rho^*} \right) + \frac{1}{\beta Re_m} \mathbf{R}_u^* \cdot \mathbf{J}^*, \quad (\text{C3})$$

$$\frac{\partial \mathbf{B}^*}{\partial t^*} = -\nabla^* \times \mathbf{E}^*, \quad (\text{C4})$$

$$\mathbf{E}^* + \mathbf{u}^* \times \mathbf{B}^* = \hat{\lambda}_i \frac{1}{\rho^*} \mathbf{J}^* \times \mathbf{B}^* - \hat{\lambda}_i \frac{\beta}{\rho^*} \nabla^* p_e^* + \frac{1}{Re_m} \mathbf{R}_u^*, \quad (\text{C5})$$

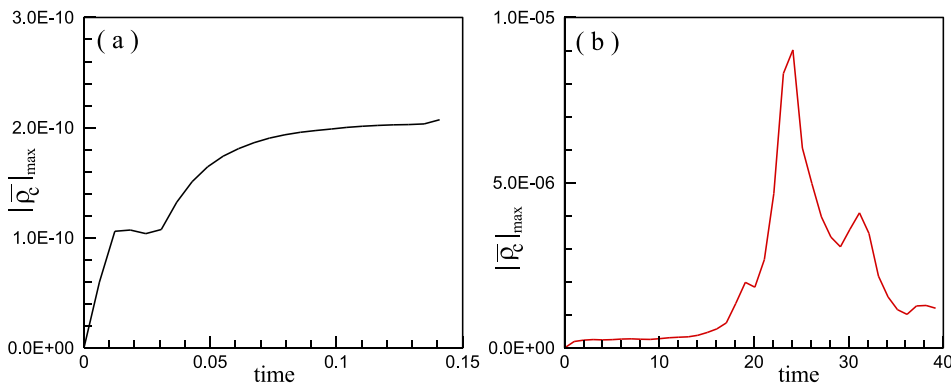


FIG. 11. The temporal variations of maximum normalized charge density for (a) plasma shock and (b) magnetic reconnection cases.

$$\mathbf{J}^* = \nabla^* \times \mathbf{B}^*. \quad (\text{C6})$$

Equations (C1)–(C6) are the conventional Hall-MHD equations^{52,54} in which \mathbf{R}_u is a function of current density, \mathbf{J}^* , as shown in Appendix A3 and $\frac{1}{\beta Re_m} \mathbf{R}_u \cdot \mathbf{J}^* \propto \frac{1}{\beta Re_m} \mathbf{J}^* \cdot \mathbf{J}^*$ represents the resistive effects. The \mathbf{q}_{te}^* and \mathbf{R}_T^* terms have been never been considered in previous derivations of Hall-MHD equations. For the tests considered in this study, these two terms are negligible. In the presence of turbulence, it is assumed that viscous dissipation does not vanish in the infinite Reynolds number limit, so that the domain of applicability of Eqs. (C1)–(C6) relates to non-turbulent flows, unless they are used in the context of turbulence modeling with added subgrid or turbulent transport models.

Written as above, the conventional Hall-MHD equations are not closed, due to the presence of the electron pressure, p_e^* , which cannot be estimated from the rest of the variables. In practice, to close the equations, some studies^{54–56} simply neglect the electron pressure, while others^{34,57} assume identical ion and electron temperatures, $T_i^* = T_e^*$. In the latter case, the electron pressure becomes $p_e^* = Z p_i^* = p^* / (1 + 1/Z)$.

2. The resistive MHD equations

In regimes where $\hat{\lambda}_i \rightarrow 0$ (and/or $\hat{r}_{Li} \rightarrow 0$), $Re^i, Re^e \rightarrow \infty$, and $Fr \rightarrow \infty$, the single-fluid equations (35)–(38) reduce to

$$\frac{\partial \rho^*}{\partial t^*} + \nabla^* \cdot (\rho^* \mathbf{u}^*) = 0, \quad (\text{C7})$$

$$\frac{\partial(\rho^* \mathbf{u}^*)}{\partial t^*} + \nabla^* \cdot (\rho^* \mathbf{u}^* \mathbf{u}^*) = -\beta \nabla^* p^* + \mathbf{J}^* \times \mathbf{B}^*, \quad (\text{C8})$$

$$\frac{1}{\gamma - 1} \left[\frac{\partial p^*}{\partial t^*} + \nabla^* \cdot (p^* \mathbf{u}^*) \right] = -p^* \nabla^* \cdot \mathbf{u}^* + \frac{1}{\beta Re_m} \mathbf{R}_u \cdot \mathbf{J}^*, \quad (\text{C9})$$

$$\frac{\partial \mathbf{B}^*}{\partial t^*} = -\nabla^* \times \mathbf{E}^*, \quad (\text{C10})$$

$$\mathbf{E}^* + \mathbf{u}^* \times \mathbf{B}^* = \frac{1}{Re_m} \mathbf{R}_u, \quad (\text{C11})$$

$$\mathbf{J}^* = \nabla^* \times \mathbf{B}^*. \quad (\text{C12})$$

Equations (C7)–(C12) are the non-dimensional resistive MHD equations^{46,54}. Obviously, the resistive MHD equations are closed without the need of explicitly assuming identical ion and electron temperatures ($T_i^* = T_e^*$). As before, \mathbf{R}_u is a function of current density, \mathbf{J}^* . Again, neglecting the viscous contributions in the infinite Reynolds number limit generally precludes the use of Eqs. (C7)–(C12) for turbulent flow calculations.

3. The ideal MHD equations

If in addition, $Re_m \rightarrow \infty$, the resistive MHD equations (C7)–(C12) can be further reduced to the ideal-MHD equations^{46,54} given as follows:

$$\frac{\partial \rho^*}{\partial t^*} + \nabla^* \cdot (\rho^* \mathbf{u}^*) = 0, \quad (\text{C13})$$

$$\frac{\partial(\rho^* \mathbf{u}^*)}{\partial t^*} + \nabla^* \cdot (\rho^* \mathbf{u}^* \mathbf{u}^*) = -\beta \nabla^* p^* + \mathbf{J}^* \times \mathbf{B}^*, \quad (\text{C14})$$

$$\frac{1}{\gamma - 1} \left[\frac{\partial p^*}{\partial t^*} + \nabla^* \cdot (p^* \mathbf{u}^*) \right] = -p^* \nabla^* \cdot \mathbf{u}^*, \quad (\text{C15})$$

$$\frac{\partial \mathbf{B}^*}{\partial t^*} = -\nabla^* \times \mathbf{E}^*, \quad (\text{C16})$$

$$\mathbf{E}^* + \mathbf{u}^* \times \mathbf{B}^* = 0, \quad (\text{C17})$$

$$\mathbf{J}^* = \nabla^* \times \mathbf{B}^*. \quad (\text{C18})$$

REFERENCES

- ¹F. F. Chen, *Introduction to Plasma Physics and Controlled Fusion* (Plenum Press, New York and London, 1984).
- ²S. Nakai and H. Takabe, "Principles of inertial confinement fusion - physics of implosion and the concept of inertial fusion energy," *Rep. Prog. Phys.* **59**, 1071–1131 (1996).
- ³S. Pfalzner, *An Introduction to Inertial Confinement Fusion* (CRC Press, 2006).
- ⁴E. R. Priest, *Solar Magnetohydrodynamics* (Spring, 1983).
- ⁵M. B. Kallenrode, *Space Physics* (Springer-Verlag, 1998).
- ⁶J. Birn, J. F. Drake, M. A. Shay, B. N. Rogers, R. E. Denton, M. Hesse, M. Kuznetsova, Z. W. Ma, A. Bhattacharjee, A. Otto, and P. L. Pritchett, "Geospace environmental modeling (GEM) magnetic reconnection challenge," *J. Geophys. Res.* **106**, 3715–3720, <https://doi.org/10.1029/1999JA900449> (2001).
- ⁷M. I. Boulos, "Thermal plasma processing," *IEEE Trans. Plasma Sci.* **19**, 1078–1089 (1991).
- ⁸J. Y. Jeong, S. E. Babayan, V. J. Tu, J. Park, I. Henins, R. F. Hicks, and G. S. Selwyn, "Etching materials with an atmospheric-pressure plasma jet," *Plasma Sources Sci. Technol.* **7**, 282–285 (1998).
- ⁹E. Gomez, D. A. Rani, C. R. Cheeseman, D. Deegan, M. Wise, and A. R. Boccaccini, "Thermal plasma technology for the treatment of wastes: A critical review," *J. Hazard Mater.* **161**, 614–626 (2009).
- ¹⁰S. A. Kaplan and V. N. Tsytovich, *Plasma Astrophysics* (Pergamon Press, 1973).
- ¹¹S. Orlando, F. Bocchino, F. Reale, G. Peres, and O. Petruk, "On the origin asymmetries in bilateral supernova remnants," *Astron. Astrophys.* **470**, 927–939 (2007).
- ¹²E. G. Zweibel and M. Yamada, "Magnetic reconnection in astrophysical and laboratory plasmas," *Annu. Rev. Astron. Astrophys.* **47**, 291–332 (2009).
- ¹³W. Kohn and L. J. Sham, "Self-consistent equations including exchange and correlation effects," *Phys. Rev.* **140**, A1133 (1965).
- ¹⁴S. X. Hu, L. A. Collins, V. N. Goncharov, J. D. Kress, R. L. McCrory, and S. Skupsky, "First-principles investigations on ionization and thermal conductivity of polystyrene for inertial confinement fusion applications," *Phys. Plasmas* **23**, 042704 (2016).
- ¹⁵Y. H. Ding, A. J. White, S. X. Hu, O. Certik, and L. A. Collins, "Ab Initio studies on the stopping power of warm dense matter with time-dependent orbital-free density functional theory," *Phys. Rev. Lett.* **121**, 145001 (2018).
- ¹⁶D. C. Montgomery and D. A. Tidman, *Plasma Kinetic Theory* (McGraw-Hill Press, 1964).
- ¹⁷S. I. Braginskii, "Transport processes in a plasma," in *Reviews of Plasma Physics*, edited by M. A. Leontovich (Consultants Bureau, New York, 1965), Vol. 1, pp. 205–311.
- ¹⁸S. Chapman and T. G. Cowling, *The Mathematical Theory of Non-Uniform Gases* (Cambridge University Press, 1970).
- ¹⁹C. Cercignani, *The Boltzmann Equation and Its Applications* (Springer-Verlag, New-York, 1988).
- ²⁰P. Amendt, S. C. Wilks, C. Bellei, C. K. Li, and R. D. Petrasso, "The potential role of electric fields and plasma barodiffusion on the inertial confinement fusion database," *Phys. Plasmas* **18**, 056308 (2011).
- ²¹G. Kagan and X. Z. Tang, "Electro-diffusion in a plasma with two ion species," *Phys. Plasmas* **19**, 082709 (2012).
- ²²L. Yin, B. J. Albright, W. Taitano, E. L. Vold, L. Chacon, and A. N. Simakov, "Plasma kinetic effects on interfacial mix," *Phys. Plasmas* **23**, 112302 (2016).

- ²³A. N. Simakov and K. Molvig, "Electron transport in a collisional plasma with multiple ion species," *Phys. Plasmas* **21**, 024503 (2014).
- ²⁴A. N. Simakov and K. Molvig, "Hydrodynamic description of an unmagnetized plasma with multiple ion species. II. Two and three ion species plasmas," *Phys. Plasmas* **23**, 032116 (2016).
- ²⁵E. L. Vold, R. M. Rauenzahn, C. H. Aldrich, K. Molvig, A. N. Simakov, and B. M. Haines, "Plasma transport in an Eulerian AMR code," *Phys. Plasmas* **24**, 042702 (2017).
- ²⁶E. L. Vold, L. Yin, W. Taitano, K. Molvig, and B. J. Albright, "Diffusion-driven fluid dynamics in ideal gases and plasmas," *Phys. Plasmas* **25**, 062102 (2018).
- ²⁷A. Sommerfeld, *Thermodynamics and Statistical Mechanics* (Academic Press, 1964).
- ²⁸S. Gershchenko and D. Livescu, "Viscous effects on the Rayleigh-Taylor instability with background temperature gradient," *Phys. Plasmas* **23**, 072121 (2016).
- ²⁹C. R. Weber, D. S. Clark, A. W. Cook, L. E. Busby, and H. F. Robey, "Inhibition of turbulence in inertial-confinement-fusion hot spots by viscous dissipation," *Phys. Rev. E* **89**, 053106 (2014).
- ³⁰T. Wei and D. Livescu, "Late-time quadratic growth in single-mode Rayleigh-Taylor instability," *Phys. Rev. E* **86**, 046405 (2012).
- ³¹R. Betti, M. Umansky, V. Lobatchev, V. N. Goncharov, and R. L. McCrory, "Hot-spot dynamics and deceleration-phase Rayleigh-Taylor instability of imploding inertial confinement fusion capsules," *Phys. Plasmas* **8**, 5257-5267 (2001).
- ³²M. J. Edwards, J. D. Lindl, B. K. Spears, S. V. Weber, L. J. Atherton, D. L. Bleuel, D. K. Bradley, D. A. Callahan, C. J. Cerjan, D. Clark, G. W. Collins et al., "The experimental plan for cryogenic layered target implosions on the National Ignition Facility-The inertia confinement approach to fusion," *Phys. Plasmas* **18**, 051003 (2011).
- ³³E. N. Parker, "Magnetic neutral sheet in evolving fields-part two-formation of the solar corona," *Astrophys. J.* **264**, 642-647 (1983).
- ³⁴P. K. Browning, A. Stanier, G. Ashworth, K. G. McClements, and V. S. Lukin, "Self-organization during spherical torus formation by flux rope merging in the mega ampere spherical tokamak," *Plasma Phys. Controlled Fusion* **56**, 064009 (2014).
- ³⁵W. Daughton, V. Roytershteyn, H. Karimabadi, L. Yin, B. J. Albright, B. Bergen, and K. J. Bower, "Role of electron physics in the development of turbulent magnetic reconnection in collisionless plasmas," *Nat. Phys.* **7**, 539-542 (2011).
- ³⁶R. Fitzpatrick, *Plasma Physics: An Introduction* (CRC Press, 2014).
- ³⁷P. Dimotakis, "The mixing transition in turbulent flows," *J. Fluid Mech.* **409**, 69-98 (2000).
- ³⁸A. W. Cook, W. H. Cabot, and P. L. Miller, "The mixing transition in Rayleigh-Taylor instability," *J. Fluid Mech.* **511**, 333-362 (2004).
- ³⁹G. L. Eyink, "Locality of turbulent cascades," *Physica D* **207**, 91-116 (2005).
- ⁴⁰D. Zhao and H. Aluie, "Inviscid criterion for decomposing scales," *Phys. Rev. Fluids* **3**, 054603 (2018).
- ⁴¹J. Ryu and D. Livescu, "Turbulence structure behind the shock in canonical shock-vortical turbulence interaction," *J. Fluid Mech.* **756**, R1 (2014).
- ⁴²D. Biskamp, E. Schwarz, and J. F. Drake, "Two-fluid theory of collisionless magnetic reconnection," *Phys. Plasmas* **4**, 1002 (1997).
- ⁴³Z. W. Ma and A. Bhattacharjee, "Hall magnetohydrodynamic reconnection: The Geospace Environment Modeling challenge," *J. Geophys. Res.* **106**, 3773-3782, <https://doi.org/10.1029/1999JA001004> (2001).
- ⁴⁴M. A. Shay, J. F. Drake, and B. N. Rogers, "Alfvénic collisionless magnetic reconnection and the Hall term," *J. Geophys. Res.* **106**, 3759-3772, <https://doi.org/10.1029/1999JA001007> (2001).
- ⁴⁵A. Hakim, J. Loverich, and U. Shumlak, "A high resolution wave propagation scheme for ideal two-fluid plasma equations," *J. Comput. Phys.* **219**, 418-442 (2006).
- ⁴⁶J. P. Freidberg, "Ideal magnetohydrodynamic theory of magnetic fusion systems," *Rev. Mod. Phys.* **54**, 801-903 (1982).
- ⁴⁷T. Ogino, "A three-dimensional MHD simulation of the interaction of the solar wind with the Earth's magnetosphere: The generation of field-aligned currents," *J. Geophys. Res.* **91**, 6791-6806, <https://doi.org/10.1029/JA091iA06p06791> (1986).
- ⁴⁸T. I. Gombosi, K. G. Powell, and D. L. De Zeeuw, "Axisymmetric modeling of cometary mass loading on an adaptively refined grid: MHD results," *J. Geophys. Res.* **99**, 21525, <https://doi.org/10.1029/94JA01540> (1994).
- ⁴⁹Z. Miki, J. A. Linker, D. D. Schnack, R. Lionello, and A. Tarditi, "Magnetohydrodynamic modeling of the global solar corona," *Phys. Plasmas* **6**, 2217-2224 (1999).
- ⁵⁰C. P. T. Groth, D. L. De Zeeuw, T. I. Gombosi, and K. G. Powell, "Global three-dimensional MHD simulation of a space weather event: CME formation, interplanetary propagation, and interaction with the magnetosphere," *J. Geophys. Res.* **105**, 25053-25078, <https://doi.org/10.1029/2000JA900093> (2000).
- ⁵¹J. F. Chapman, I. H. Cairns, J. G. Lyon, and C. R. Boshuizen, "MHD simulations of Earth's bow shock: Interplanetary magnetic field orientation effects on shape and position," *J. Geophys. Res.* **109**, A04215, <https://doi.org/10.1029/2003JA010235> (2004).
- ⁵²J. D. Huba, "Hall magnetohydrodynamics-A tutorial," in *Space Plasma Simulation*, Lecture Notes in Physics, edited by J. Büchner, C. Dum, and M. Scholer (Springer Verlag, Berlin, 2003), Vol. 615, pp. 166-192.
- ⁵³A. Otto, "Geospace environmental modeling (GEM) magnetic reconnection challenge: MHD and Hall MHD constant and current dependent resistivity models," *J. Geophys. Res.* **106**, 3751-3757, <https://doi.org/10.1029/1999JA001005> (2001).
- ⁵⁴J. D. Callen, *Fundamentals of Plasma Physics* (University of Wisconsin, 2006).
- ⁵⁵P. Dmitruk and W. H. Matthaeus, "Structure of the electromagnetic field in the three-dimensional Hall magnetohydrodynamic turbulence," *Phys. Plasmas* **13**, 0423073 (2006).
- ⁵⁶G. Toth, Y. Ma, and T. I. Gombosi, "Hall magnetohydrodynamics on block-adaptive grids," *J. Comput. Phys.* **227**, 6967-6984 (2008).
- ⁵⁷B. Srinivasan and U. Shumlak, "Analytical and computational study of the ideal full two-fluid plasma model and asymptotic approximations for Hall-magnetohydrodynamics," *Phys. Plasmas* **18**, 092113 (2011).
- ⁵⁸Y. J. Ma, C. T. Russell, A. F. Nagy, G. Toth, M. K. Dougherty, A. Wellbrock, A. J. Coates, P. Garnier, J. E. Wahlund, T. E. Cravens, M. S. Richard, and F. J. Crary, "The importance of thermal electron heating in Titan's ionosphere: Comparison with Cassini T34 flyby," *J. Geophys. Res.: Space Phys.* **116**, A10213, <https://doi.org/10.1029/2011JA016657> (2011).
- ⁵⁹U. Shumlak and J. Loverich, "Approximate Riemann solver for the two-fluid plasma model," *J. Comput. Phys.* **187**, 620-638 (2003).
- ⁶⁰D. Bond, V. Wheatly, R. Samtaney, and D. I. Pullin, "Richtmyer Meshkov instability of a thermal interface in a two-fluid plasma," *J. Fluid Mech.* **833**, 332-363 (2017).
- ⁶¹J. Loverich, A. Hakim, and U. Shumlak, "A discontinuous Galerkin method for ideal two-fluid plasma equations," *Commun. Comput. Phys.* **9**, 240-268 (2011).
- ⁶²A. Dubey, K. Antypas, M. K. Ganapathy, L. B. Reid, K. Riley, D. Sheeler, A. Siegel, and K. Weide, "Extensible component based architecture for flash, a massively parallel, multiphysics simulation code," *Parallel Comput.* **35**, 512-522 (2009).
- ⁶³P. Tzeferacos, M. Fatenejad, N. Flocke, C. Graziani, G. Gregori, D. Lamb, D. Lee, J. Meinecke, A. Scopatz, and K. Weide, "FLASH MHD simulations of experiments that study shock-generated magnetic fields," *High Energy Density Phys.* **17**, 24 (2015).
- ⁶⁴M. M. Marinak, S. W. Hann, T. R. Dittrich, R. E. Tipton, and G. B. Zimmerman, "A comparison of three-dimensional multimode hydrodynamic instability growth on various national ignition facility capsule designs with hydra simulations," *Phys. Plasmas* **5**, 1125-1132 (1998).
- ⁶⁵M. M. Marinak, G. D. Kerbel, N. A. Gentile, O. Jones, D. Munro, S. Pollaine, T. R. Dittrich, and S. W. Hann, "Three-dimensional hydra simulations of national ignition facility targets," *Phys. Plasmas* **8**, 2275-2280 (2001).
- ⁶⁶A. W. Cook, "Artificial fluid properties for large-eddy simulation of compressible turbulent mixing," *Phys. Fluids* **19**, 055103 (2007).
- ⁶⁷C. R. Weber, D. S. Clark, A. W. Cook, D. C. Eder, S. W. Haan, B. A. Hammel, D. E. Hinkel, O. S. Jones, M. M. Marinak, J. L. Milovich, P. K. Patel, H. F. Robey, J. D. Salmonson, S. M. Sepke, and C. A. Thomas, "Three-

- dimensional hydrodynamics of the deceleration stage in inertial confinement fusion," *Phys. Plasmas* **22**, 032702 (2015).
- ⁶⁸Y. T. Lee and R. M. More, "An electron conductivity model for dense plasmas," *Phys. Fluids* **27**, 1273–1286 (1984).
- ⁶⁹M. S. Murillo, "Viscosity estimates of liquid metals and warm dense matter using the Yukawa reference system," *High Energy Density Phys.* **4**, 49–57 (2008).
- ⁷⁰S. K. Lele, "Compact finite difference schemes with spectral-like resolution," *J. Comput. Phys.* **103**, 16–42 (1992).
- ⁷¹L. Burakovsky, C. Ticknor, J. D. Kress, and L. A. Collins, "Transport properties of lithium hydride at extreme conditions from orbital-free molecular dynamics," *Phys. Rev. E* **87**, 023104 (2013).
- ⁷²S. X. Hu, L. A. Collins, T. R. Boehly, J. D. Kress, V. N. Goncharov, and S. Skupsky, "First-principles thermal conductivity of warm-dense deuterium plasmas for inertial confinement fusion applications," *Phys. Rev. E* **89**, 043105 (2014).
- ⁷³J. R. Rygg, F. H. Sguin, C. K. Li, J. A. Frenje, M. J.-E. Manuel, R. D. Petrasso, R. Betti, J. A. Delettrez, O. V. Gotchev, J. P. Knauer, D. D. Meyerhofer, F. J. Marshall, C. Stoeckl, and W. Theobald, "Proton radiography of inertial fusion implosions," *Science* **319**, 1223–1225 (2008).
- ⁷⁴D. Livescu, J. Mohd-Yusof, M. R. Petersen, and J. W. Grove, "CFDNS: A computer code for direct numerical simulation of turbulent flows," Technical Report LA-CC-09-100 (Los Alamos National Laboratory, 2009).
- ⁷⁵M. R. Petersen and D. Livescu, "Forcing for statistically stationary compressible isotropic turbulence," *Phys. Fluids* **22**, 116101 (2010).
- ⁷⁶S. Tomczyk, S. W. McIntosh, S. L. Keil, P. G. Judge, D. H. S. T. Schad, and J. Edmondson, "Alfvén waves in the solar corona," *Science* **317**, 1192–1196 (2007).
- ⁷⁷R. L. Stenzel, "Whistler waves in space and laboratory plasmas," *J. Geophys. Res.* **104**, 14379–14396, <https://doi.org/10.1029/1998JA900120> (1999).
- ⁷⁸P. A. Cassak and M. A. Shay, "Magnetic reconnection for coronal conditions: Reconnection rates, secondary islands and onset," *Space Sci. Rev.* **172**, 283–302 (2012).
- ⁷⁹S. M. Bellan, *Fundamentals of Plasma Physics* (Cambridge University Press, 2006).
- ⁸⁰M. E. Mandt, R. E. Denton, and J. F. Drake, "Transition to whistler mediated magnetic reconnection," *Geophys. Res. Lett.* **21**, 73–76, <https://doi.org/10.1029/93GL03382> (1994).
- ⁸¹L. Wang, A. H. Hakim, A. Bhattacharjee, and K. Germaschewski, "Comparison of multi-fluid moment models with particle-in-cell simulations of collisionless magnetic reconnection," *Phys. Plasmas* **22**, 012108 (2015).
- ⁸²W. Shen and M. Dryer, "Magnetohydrodynamic theory for the interaction of interplanetary double-shock ensemble with the Earth's bow shock," *J. Geophys. Res.* **77**, 4627–4644, <https://doi.org/10.1029/JA077i025p04627> (1972).
- ⁸³M. Peredo, J. A. Slavin, E. Mazur, and S. A. Curtis, "Three-dimensional position and shape of the bow shock and their variation with Alfvénic, sonic and magnetosonic Mach numbers and interplanetary magnetic field orientation," *J. Geophys. Res.* **100**, 7907–7916, <https://doi.org/10.1029/94JA02545> (1995).
- ⁸⁴M. Brio and C. C. Wu, "An upwind differencing scheme for the equations of ideal magnetohydrodynamics," *J. Comput. Phys.* **75**, 400–422 (1988).
- ⁸⁵L. Mejnertsen, J. P. Eastwood, H. Hietala, S. J. Schwartz, and J. P. Chittenden, "Global MHD simulations of the Earth's bow shock shape and motion under variable Solar wind conditions," *J. Geophys. Res.* **123**, 259–271, <https://doi.org/10.1002/2017JA024690> (2018).
- ⁸⁶G. S. Jiang and C. C. Wu, "A high-order WENO finite difference scheme for the equations of ideal magnetohydrodynamics," *J. Comput. Phys.* **150**, 561–594 (1999).
- ⁸⁷H. C. Yee, D. V. Kotov, W. Wang, and C. W. Shu, "Spurious behavior of shock-capturing methods by the fractional step approach: Problems containing stiff source and discontinuities," *J. Comput. Phys.* **241**, 266–291 (2013).
- ⁸⁸J. A. Greenough and W. J. Rider, "A quantitative comparison of numerical methods for the compressible Euler equations: Fifth-order WENO and piecewise-linear Godunov," *J. Comput. Phys.* **196**, 259–281 (2004).
- ⁸⁹T. Nagai, I. Shinohara, M. Fujimoto, M. Hoshino, Y. Saito, S. Machida, and T. Mukai, "Geotail observation of the Hall current system: Evidence of magnetic reconnection in the magnetotail," *J. Geophys. Res.* **106**, 25929–25949, <https://doi.org/10.1029/2001JA900038> (2001).
- ⁹⁰X. H. Deng and H. Matsumoto, "Rapid magnetic reconnection in the Earth's magnetosphere mediated by whistler waves," *Nature* **410**, 557–560 (2001).
- ⁹¹J. A. Wesson, "Sawtooth reconnection," *Nucl. Fusion* **30**, 2545 (1990).
- ⁹²P. K. Browning, S. Cardnell, M. Evans, F. Arese Lucini, V. S. Lukin, K. G. McClements, and A. Stainer, "Two-fluid and magnetohydrodynamic modelling of magnetic reconnection in the MAST of magnetic reconnection in the MAST spherical tokamak and the solar corona," *Plasma Phys. Controlled Fusion* **58**, 015041 (2016).
- ⁹³L. G. Stanton and M. S. Murillo, "Ion transport in high-energy-density matter," *Phys. Rev. E* **93**, 043202 (2016).